

University of Central Florida

STARS

Electronic Theses and Dissertations

2007

Zinc Cadmium Sulphide And Zinc Sulphide As Alternative Heterojunction Partners For Cigs2 Solar Cells

Bhaskar Kumar

University of Central Florida



Part of the [Materials Science and Engineering Commons](#)

Find similar works at: <https://stars.library.ucf.edu/etd>

University of Central Florida Libraries <http://library.ucf.edu>

This Masters Thesis (Open Access) is brought to you for free and open access by STARS. It has been accepted for inclusion in Electronic Theses and Dissertations by an authorized administrator of STARS. For more information, please contact STARS@ucf.edu.

STARS Citation

Kumar, Bhaskar, "Zinc Cadmium Sulphide And Zinc Sulphide As Alternative Heterojunction Partners For Cigs2 Solar Cells" (2007). *Electronic Theses and Dissertations*. 3234.

<https://stars.library.ucf.edu/etd/3234>

ZINC CADMIUM SULPHIDE AND ZINC SULPHIDE AS ALTERNATIVE
HETEROJUNCTION PARTNERS FOR CIGS₂ SOLAR CELLS

by

BHASKAR KUMAR

B.Tech Indian Institute of Technology Madras, 2005

A thesis submitted in partial fulfillment of the requirements
for the degree of Master of Science
in the Department of Mechanical, Materials and Aerospace Engineering
in the College of Engineering and Computer Science
at the University of Central Florida
Orlando, Florida

Fall Term
2007

Major Professor: Neelkanth G Dhere

© 2007 Bhaskar Kumar

ABSTRACT

Devices with ZnCdS/ZnS heterojunction partner layer have shown better blue photon response due to higher band gap of these compounds as compared to devices with CdS heterojunction partner layer. CdS heterojunction partner layer has shown high photovoltaic conversion efficiencies with CIGS absorber layer while efficiencies are lower with $\text{CuIn}_{1-x}\text{Ga}_x\text{S}_2$ (CIGS2). A negative conduction band offset has been observed for CdS/CIGS2 as compared to near flat conduction band alignment in case of CdS/CIGS devices, which results in higher interface dominated recombination. Moreover, it has been predicted that optimum band offsets for higher efficiency solar cells may be achieved for cells with alternative heterojunction partner such as ZnS. With varying ratio of Zn/ (Zn+Cd) in $\text{Zn}_x\text{Cd}_{1-x}\text{S}$ a range of bandgap energies can be obtained and thus an optimum band offset can be engineered. For reducing interface dominated recombination better lattice match between absorber and heterojunction partners is desirable. Although CdS has better lattice match with $\text{CuIn}_{1-x}\text{Ga}_x\text{S}_2$ absorber layer, same is not true for $\text{CuIn}_{1-x}\text{Ga}_x\text{S}_2$ absorber layers. Utilizing $\text{Zn}_x\text{Cd}_{1-x}\text{S}$ as heterojunction partner provides a range of lattice constant (between $a_{\text{ZnS}} = \sim 5.4 \text{ \AA}$ and $a_{\text{CdS}} = \sim 5.7 \text{ \AA}$) depending on Zn/(Zn+Cd). Therefore better lattice match can be obtained between heterojunction partner and absorber layer. Better lattice match will lead to lower interface dominated recombination, hence higher open circuit voltages.

In the present study chemical bath deposition parameters are near optimized for high efficiency CIGS2 Solar cells. Effect of various chemical bath deposition parameters on device performance was studied and attempts were made to optimize the deposition parameters in order to improve the device performance. In/(In+Ga) ratio in absorber layer is varied to obtain good

lattice match and optimum band alignment. Solar cells with conversion efficiencies comparable to conventional CdS/CIGS2 has been obtained with $Zn_xCd_{1-x}S$ /CIGS2. High short current as well as higher open circuit voltages were obtained with $Zn_xCd_{1-x}S$ as alternative heterojunction partner for CIGS2 solar cells as compared to SLG/Mo/CIGS2/ CdS / i-ZnO/ZnO:Al.

Dedicated to
Lord Badri Vishal
&
My beloved Parents

ACKNOWLEDGMENTS

First and foremost, I would like to take this opportunity to thank my advisor, Dr. Neelkanth G. Dhere, for his help and support throughout this work. I enjoyed working under his supervision and appreciate his constant guidance and encouragement. It really was a great experience and an overall growth of personality. I would like to thank Dr. Christine Klemenz, Dr. Kalpathy B Sundaram and Dr. Helge Heinrich for serving on my final examination committee and for their invaluable suggestions.

This research is supported by National Renewable Energy Laboratory (NREL). I would like to thank Dr. James Sites and his colleagues at Colorado State University for LBIC and C-V measurements. A special word of thanks goes to Kirk Scammon from AMPAC's Materials Characterization Facility (MCF).

I would like to acknowledge the help of following colleagues during this project: Shirish Pethe, Sachin Kulkarni, Vinaykumar Hadagali, Parag Vasekar, Ashwani Kaul and others at the Florida Solar Energy Center. I thank Dipika Darshana and all my friends at UCF for their timely help and support.

Words cannot truly express my deepest gratitude and appreciation to my parents, brothers and family members, who always gave me their love and emotional support.

TABLE OF CONTENTS

LIST OF FIGURES	ix
LIST OF ACRONYMS/ABBREVIATIONS	xiii
1 INTRODUCTION.....	1
2 PHYSICS OF SOLAR CELLS.....	3
2.1 p-n Junctions	5
2.1.1 <i>Homojunctions</i>	5
2.1.2 <i>Heterojunctions</i>	7
2.2 Solar Cells.....	9
2.2.1 <i>Solar Spectrum</i>	9
2.2.2 <i>p-n Junction Solar Cells</i>	10
2.2.3 <i>Quantum efficiency</i>	16
3 CHALCOPYRITE SOLAR CELLS.....	17
3.1 Chalcopyrite absorber layer	19
3.2 Need and selection of heterojunction partners.....	21
3.3 Heterojunction materials used in I-III-VI ₂ Solar cells	22
3.4 Cadmium sulfide.....	25
3.5 Zinc sulfide	28
3.6 Zinc cadmium sulfide	29
3.7 Chemical bath deposition technique	29
4 EXPERIMENTAL TECHNIQUE	31

4.1	Chemical Bath Deposition Technique:	31
4.2	Chemistry of Bath.....	32
5	RESULTS AND DISCUSSIONS.....	34
5.1	Effects of variation of deposition parameters on device performance	35
5.1.1	<i>Influence of deposition time.....</i>	<i>36</i>
5.1.2	<i>Influence of ammonium hydroxide concentration.....</i>	<i>41</i>
5.1.3	<i>Effect of cadmium sulfate concentration.....</i>	<i>44</i>
5.1.4	<i>Zinc sulfate concentration variation.....</i>	<i>47</i>
5.1.5	<i>Thiourea concentration variation.....</i>	<i>49</i>
5.1.6	<i>Effect of annealing of $Zn_xCd_{1-x}S$ layer after deposition.....</i>	<i>51</i>
5.2	Effect of Indium concentration variation in the absorber layer	52
5.3	Comparison of CIGS2/ $Zn_xCd_{1-x}S$ and CdS/CIGS2 solar cell.....	56
5.4	Light-Beam-Induced Current (LBIC) Analysis	60
5.5	Capacitance-Voltage Measurement	61
6	CONCLUSIONS AND RECOMMENDATIONS.....	63
	REFERENCE.....	66

LIST OF FIGURES

Figure 2.1: Energy band diagram of a p-n homojunctions.	5
Figure 2.2: (a) Metallurgical junction between p and n -type semiconductors (b) Space charge region distribution at thermal equilibrium (c) Electric field distribution (d) Potential distribution	7
Figure 2.3: Schematic Anderson heterojunction with positive ΔE_C and ΔE_V	8
Figure 2.4: illustration of solar radiation spectrum AM_m . Where m stands for $\sec(z)$	10
Figure 2.5: Standard AM1.5 solar spectrum.	10
Figure 2.6: A typical band diagram of CIGS/CdS Solar cell.....	11
Figure 2.7: Ideal current-Voltage characteristics of a solar cell in the dark and under illumination.	12
Figure 2.8: Equivalent circuit diagram for a solar cell (a) ideal solar cell in the dark and under illuminated condition (b) non-ideal solar cell with series and shunt resistance in the dark and under illuminated condition.	13
Figure 2.9: Effect of series resistance on short circuit current.	14
Figure 2.10: Effect of shunt resistance on open circuit voltage.....	15
Figure 2.11: Quantum efficiency plot showing various losses in solar cell	16
Figure 3.1: Schematic representation of the standard structure of the chalcopyrite solar cell	17
Figure 3.2 Dependence of the absorption coefficient on photon energy [19].	19
Figure 3.3: chalcopyrite structure [21]......	20
Figure 3.4: Zinc blende structure	23
Figure 3.5: Wurtzite structure	24

Figure 3.6: AM1.5 Solar Spectrum and maximum attainable short circuit current density with various band gap energies.....	26
Figure 3.7 Schematic band diagram for CIGS2/CdS interface [29].....	27
Figure 3.8 Schematic diagram of the interface of two single crystal with different lattice parameters, resulting in formation of edge dislocation.....	28
Figure 4.1: Experimental setup for chemical bath deposition	31
Figure 4.2: Schematic diagram showing various stages in cluster mechanism for Zinc sulfide growth.....	33
Figure 5.1: Differential Auger spectra of $Zn_xCd_{1-x}S$ thin film deposited on $SnO_2:F$ glass	35
Figure 5.2: Optical transmittance spectra for (a) $Zn_xCd_{1-x}S$ thin film deposited in a single 15 minute run (b) $Zn_xCd_{1-x}S$ layer prepared in two 15 minute depositions (c) $Zn_xCd_{1-x}S$ layer deposited in three 15 minute runs (d) standard CdS layer deposited on $SnO_2:F$ glass.....	37
Figure 5.3 The J-V characteristics for CIGS2/ $Zn_xCd_{1-x}S$ solar cells using ZnCdS layers having total deposition times of 15, 30 and 40 minutes respectively and CIGS2/CdS solar cells under AM 1.5 condition measured at FSEC.	38
Figure 5.4: X-ray diffraction pattern of $Zn_xCd_{1-x}S$ film deposited on tin oxide coated glass substrate.	39
Figure 5.5: XPS spectra for ZnS and $Zn_xCd_{1-x}S$ thin films deposited on CIGS2 film.	40
Figure 5.6: Cd $3d_{5/2}$ peak in the XPS spectrum of a $Zn_xCd_{1-x}S$ layer. Curve fitting to show contribution of CdS, $Cd(OH)_2$ and CdO_2 peaks to corresponding XPS peak is also plotted.	40
Figure 5.7: Open circuit voltage and short circuit current density values for various pH of bath controlled by NH_4OH concentrations.....	42

Figure 5.8: SEM micrographs for of the surface of $Zn_xCd_{1-x}S$ film deposited on $SnO_2:F$ glass, with NH_4OH concentration of 0.09 M during chemical bath deposition.	42
Figure 5.9: SEM micrographs of the surface of $Zn_xCd_{1-x}S$ film deposited on $SnO_2:F$ glass, with NH_4OH concentration of 0.027M during chemical bath deposition.....	43
Figure 5.10 The J-V characteristics taken at FSEC for CIGS2/ $Zn_xCd_{1-x}S$ prepared at various values of pH of bath adjusted using NH_4OH concentration.	43
Figure 5.11: Optical transmittance spectra for $Zn_xCd_{1-x}S$ films for varying $CdSO_4$ concentration, (a) 0.0001M (b) 0.0002M (c) 0.0004M	45
Figure 5.12: SEM micrographs for of the surface of $Zn_xCd_{1-x}S$ film deposited on $SnO_2:F$ glass, for $CdSO_4$ concentration of 0.0001M during chemical bath deposition.....	45
Figure 5.13: SEM micrographs for of the surface of $Zn_xCd_{1-x}S$ film deposited on $SnO_2:F$ glass, for $CdSO_4$ concentration of 0.0003M during chemical bath deposition.....	46
Figure 5.14: The J-V characteristics taken at FSEC for CIGS2/ $Zn_xCd_{1-x}S$ device deposited with various $CdSO_4$ concentrations.	46
Figure 5.15: Optical transmittance spectra for a single layer deposition of $Zn_xCd_{1-x}S$ films with varying $ZnSO_4$ concentration, (a) 0.04 M (b) 0.02M (c) 0.01 M	48
Figure 5.16: SEM micrographs for of the surface of $Zn_xCd_{1-x}S$ film deposited on $SnO_2:F$ glass, for $ZnSO_4$ concentration of (a) 0.01M (b) 0.04M during chemical bath deposition.	48
Figure 5.17: The J-V characteristics taken at FSEC for CIGS2/ $Zn_xCd_{1-x}S$ for various concentration of $ZnSO_4$ in chemical bath.	49
Figure 5.18: Optical transmittance spectra for a single layer deposition of $Zn_xCd_{1-x}S$ films with varying thiourea concentration, (a) 0.375 M (b) 0.25 M (c) 0.125 M	50

Figure 5.19: The J-V characteristics taken at FSEC for as grown and post annealed CIGS2/ Zn _x Cd _{1-x} S device.....	51
Figure 5.20: The J-V characteristics taken at FSEC for as grown and post annealed CIGS2/ Zn _x Cd _{1-x} S device.....	52
Figure 5.21 The J-V characteristics taken at FSEC for CIGS2/ Zn _x Cd _{1-x} S device formed with various sputtering time for In metallic precursor deposition for absorber layer formation (a) 90 seconds /inch (b) 80 seconds /inch (c) 70 seconds /inch (d) 60 seconds/inch	54
Figure 5.22: X-ray diffraction pattern (θ-2θ) for CIGS2 absorber layer and CIGS2/Zn _x Cd _{1-x} S layer.....	56
Figure 5.23: The J-V characteristics for SLG/Mo/CIGS2/ Zn _x Cd _{1-x} S / i-ZnO/ZnO:Al device (#1657CZ) measured at NREL After 10 minute soak at P _{max} , 5 minute cool.....	58
Figure 5.24: The J-V characteristics for SLG/Mo/CIGS2/ CdS / i-ZnO/ZnO:Al device ((#1657C) measured at NREL After 10 minute soak at P _{max} , 5 minute cool.....	59
Figure 5.25: Qunatum efficiency plot obtained at NREL for SLG/Mo/CIGS2/ CdS / i- ZnO/ZnO:Al (#1657C) and SLG/Mo/CIGS2/ Zn _x Cd _{1-x} S / i-ZnO/ZnO:Al (#1657CZ) cells.	60
Figure 5.26: LBIC measurements for for SLG/Mo/CIGS2/Zn _x Cd _{1-x} S/i-ZnO/ZnO:Al devices (#1657CZ) performed with 638-nm laser measured at Colorado State University.	61
Figure 5.27: shows C ⁻² dependence on voltage. This analysis was carried out at Colorado State University.....	62

LIST OF ACRONYMS/ABBREVIATIONS

ACRONYM	Definition of Acronym
CIS	Copper Indium Diselenide
CIGS	Copper Indium Gallium Diselenide
CIGS ₂	Copper Indium Gallium Disulfide
CIGSS	Copper Indium Gallium Selenide Sulfide
CdS	Cadmium Sulfide
ZnS	Zinc Sulfide
i:ZnO	intrinsic Zinc Oxide
ZnO:Al	Aluminum doped Zinc Oxide
Cu	Copper
In	Indium
Ga	Gallium
Se	Selenium
S	Sulfur
Mo	Molybdenum
FCC	Face Centered Cubic
J	Current Density (mA/cm ²)
J ₀	Reverse Saturation Current Density (mA/cm ²)
Q	Electronic Charge, 1.6×10^{-19} C
A	Diode Ideality Factor
K	Boltzmann's Constant, 8.61×10^{-5} eV/°C

J_D	Dark Current Density (ma/cm ²)
R_s	Series Resistance (Ohm)
R_p	Shunt or Parallel Resistance (Ohm)
V	Biased Voltage (Volts)
J_{ph}	Photo generated Current Density (mA/cm ²)
J_m	Maximum Current Density (mA/cm ²)
V_m	Maximum Voltage (Volts)
W_d	Depletion Width
V_{oc}	Open Circuit Voltage (Volts)
J_{sc}	Short Circuit Current Density (mA/cm ²)
FF	Fill Factor (%)
P_s	Irradiated Power Density (mW/cm ²)
H	Efficiency (%)
V_{bi}	Built-in Voltage (Volts)
kV	kilo volts
eV	electron volts
EPMA	Electron Probe Micro Analysis
SEM	Scanning Electron Microscopy
AES	Auger Electron Spectroscopy
XEDS	X-ray Energy Dispersive Spectroscopy
XRD	X-ray diffraction
XPS	X-ray Photoelectron Spectroscopy
QE	Quantum Efficiency

nm	nano meter (10^{-9} meter)
μm	micro meter (10^{-6} meter)
$^{\circ}\text{C}$	degree celsius

1 INTRODUCTION

World annual energy consumption is predicted to reach 30 terawatt-years (TWyr) by 2050 as compared to current 13 TWyr. On the other hand, the world is heading towards global energy crisis due to a decline in the availability of oil, and increasing carbon dioxide emissions that are causing global warming. This has enhanced interest in the development of clean renewable resources of energy production. Some of the major contenders for alternative energy resources are hydroelectric, tidal, nuclear and solar energy. 14 TWyr solar energy is incident on the globe just in one hour. Thus solar has great potential to meet a large fraction of future needs.

Photovoltaic (PV) cell is a semiconductor device that generates electricity when it is illuminated. Although the French scientist Edmund Becquerel observed photovoltaic effect in 1839, it was not fully comprehended until the development of quantum theory and solid state physics in early to middle 1900s. Since its first viable use in powering orbital satellites of the US space programs in the 1950s, photovoltaics have made significant progress with total U.S. photovoltaic module and cell shipments reaching \$131 million dollars in 1996. During the last decade, world production of PV cells/modules has been increasing at $>35\% \text{ yr}^{-1}$, exceeding >2 GW in 2006

The main barrier impeding the expansion of the terrestrial application of photovoltaics is the high cost of the solar systems. Historically, crystalline silicon (c-Si) has been the light-absorbing semiconductor in most solar cells, even though it is a relatively poor absorber of light and requires considerable thickness (several hundred microns) of material. The high cost of crystalline silicon wafers (which makes up 40-50% of the cost of a finished module) has led the industry to look for cheaper materials to make solar cells. thin film solar cells have the potential

to become an economically competitive energy source because they can be produced by low cost deposition techniques on inexpensive substrates with lower material usage. The most common materials are amorphous hydrogenated silicon (a-Si:H), and the polycrystalline materials: cadmium telluride (CdTe) and copper indium-gallium diselenide (CIGS).

Polycrystalline thin films can also be more forgiving of minute amounts of impurities in the material due to feedstock or relaxed manufacturing standards compared to single-crystal devices. Thin films are also tolerant to, “imperfect” boundaries between the crystallites, whereas single-crystal devices typically demand significant consistency from one unit cell to the next. Such tolerances result in thin-films being more amenable to large-scale production. While all thin-films share these benefits, polycrystalline thin-film cells currently have the benefit of greater stability than the amorphous-silicon thin-film cells.

At present, research is concentrated on a-Si:H, CdTe, and CIGS thin film solar cells and modules as major contenders for large-scale production.

2 PHYSICS OF SOLAR CELLS

In an isolated atom, the electrons can have only discrete energy levels as described by the Bohr atom model. When N atoms are brought together to form a crystal, the N-fold degenerate energy level splits in N separate and closely spaced energy levels consistent with Pauli exclusion principle. A further reduction in lattice spacing causes energy bands to merge and split again into two bands containing 4N bands each. These bands may overlap or may be separated by a region, which designates energies that an electron in solid cannot possess. At absolute zero, the lower band is completely filled and known as the valence band. The upper band is totally empty and labeled as the conduction band.

In conductors, the conduction band overlaps with the valence band so that the electrons can accelerate in the material leading to high electric conductivities. In the insulators, the bandgap is very large and hence electrons cannot be easily excited from the valence band to conduction band, making the material highly insulating. In semiconductors, the bandgap is not as large as in the insulators usually it is less than 3 eV, allowing the electrons to be excited from valence band to conduction band by thermal vibrations or by energetic photons.

The probability that an energy state with energy E being occupied with an electron is given by the Fermi distribution function

$$F(E) = 1/(1+e^{(E-E_F)/kT}).....2.1$$

where k is the Boltzmann constant, T is the absolute temperature, E_F is the Fermi energy.

The Fermi level is defined as the energy level where the probability of finding an electron is half. It can also be defined as the energy level below which all states will have at most two electrons of opposite spin according to Pauli exclusion principle.

$$E_F = (E_C + E_V)/2 + kT \ln(N_C/N_V)/2 \dots \dots \dots 2.2$$

where E_C is the lowest energy level in the conduction band, E_V is the highest energy level of the valence band, N_C and N_V are the effective density of state in the conduction band and valence band respectively.

Besides the temperature, the conductivity of a semiconductor is generally sensitive to, magnetic field, illumination and minute amount of impurity atoms. Semiconductors are classified in two categories: intrinsic and extrinsic. At finite temperatures, thermal vibrations can excite electrons from the valence band to the conduction band and leave a hole in valence band. Intrinsic semiconductor has low concentration of active impurities as compared to thermally excited electrons. An extrinsic semiconductor is doped with donor or acceptor impurities. When a semiconductor is doped with a donor impurity, it has an extra electron, which makes it a negative carrier type i.e. an n-type semiconductor. Similarly, when an acceptor impurity is added it gives rise to extra holes resulting in a positive carrier type i.e. p-type semiconductor. This facility of semiconductors assuming a negative or positive charge carrier type makes it one of the most important materials for development of electronic devices.

2.1 p-n Junctions

When p-type and n-type material are kept in close contact a p-n junction is formed. Since several types of solar cells are p-n junctions, a precise understanding of p-n junction is crucial for good understanding of a solar cell. The p-n junctions can be classified as homojunctions and heterojunctions.

2.1.1 Homojunctions

Homojunctions are junctions between two portions of same material one doped n-type and other doped p-type. A band diagram of a typical homojunction is shown in Figure 2.1, where E_{vac} is the vacuum level, E_C is conduction band bottom edge, E_V is valence band top edge, E_F is the Fermi level, E_g is the energy band gap, χ_s is the electron affinity of the semiconductor (Please correct elsewhere), V_d is the diffusion potential and Φ_1 and Φ_2 are the work functions for p and n side respectively.

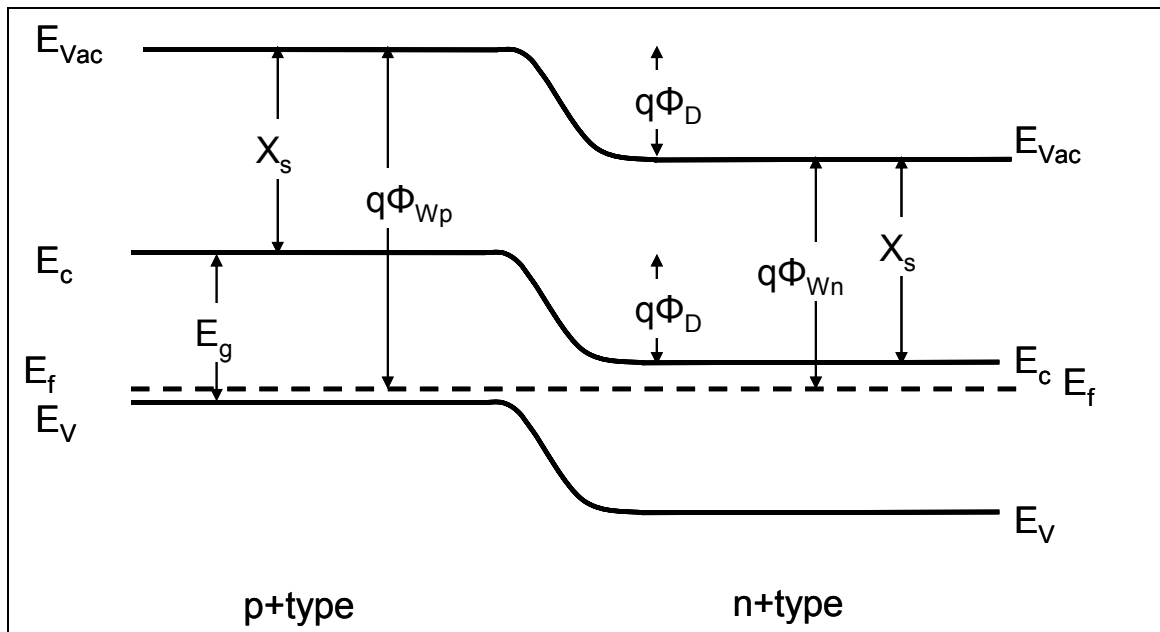


Figure 2.1: Energy band diagram of a p-n homojunctions.

Since the work functions are different on p and n sides, there exists an internal electric field leading to band bending. Diffusion potential V_d ($V_d = \Phi_1 - \Phi_2$) results in electron flow from n-type to p-type in order to equalize Fermi level on both sides when junction is formed leading to positively charged ionized donors near the interface on n-type side and negatively charged ionized acceptors near the interface on p-type side.

$$V_d = (kT/q) \ln(N_A N_D / n_i^2) \dots\dots\dots 2.3$$

Where N_A and N_D are acceptor and donor concentration respectively and n_i is the intrinsic concentration. To a good approximation depletion edges at x_n and x_p can be considered to be abrupt. Overall charge neutrality must still hold.

$$N_D x_n = N_A x_p \dots\dots\dots 2.4$$

The total space charge region width is given by

$$W_d = [2\epsilon_s V_d [N_A N_D / (N_A + N_D)] / q]^{1/2} \dots\dots\dots 2.5$$

The resulting space charge region distribution at thermal equilibrium, electric field distribution and potential distribution is shown in Figure 2.2.

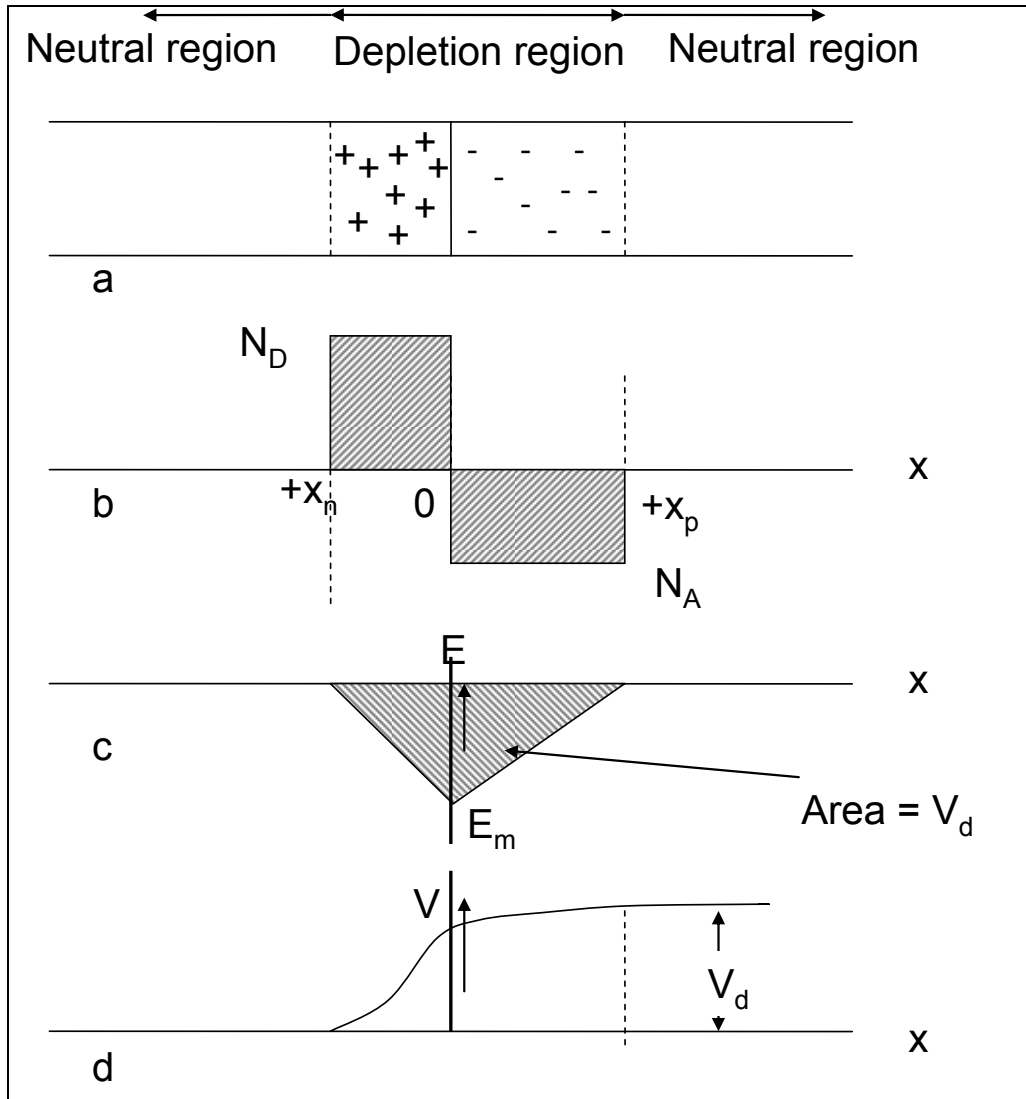


Figure 2.2: (a) Metallurgical junction between p and n -type semiconductors (b) Space charge region distribution at thermal equilibrium (c) Electric field distribution (d) Potential distribution

2.1.2 Heterojunctions

A heterojunction is formed when two semiconductors of p and n-type are placed in intimate contact on atomic level. Typically, the two semiconductors would have different band gaps and electron affinities. The heterojunctions may have a discontinuity between valence and

conduction bands, which forms due to electron affinity mismatch between the two semiconductors. Anderson model incorporates discontinuities in material properties as ϵ_s , χ , and E_g across an abrupt metallurgical junction interface. Anderson's model disregards the presence of recombination-generation in depletion region, interface states and dipoles.

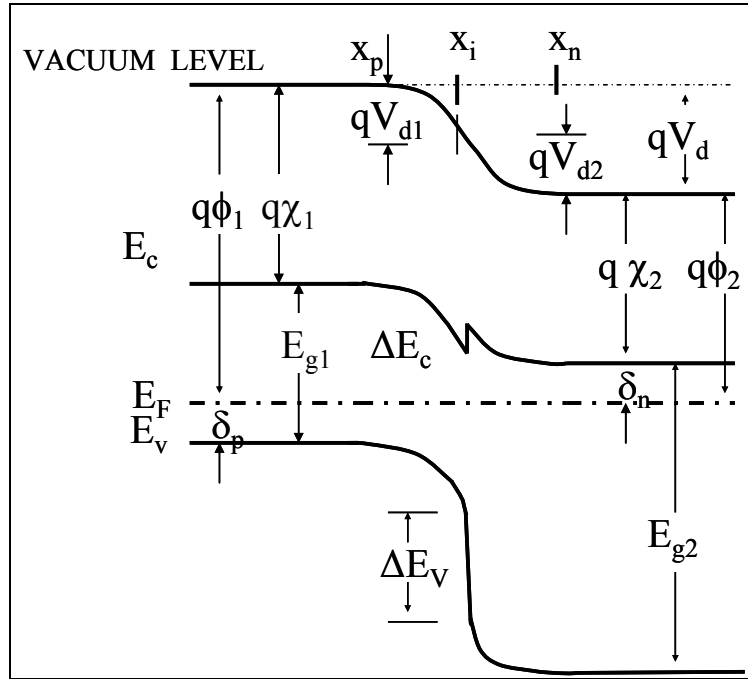


Figure 2.3: Schematic Anderson heterojunction with positive ΔE_C and ΔE_V

$$\Delta E_C = (\chi_2 - \chi_1) \dots \dots \dots 2.6$$

$$\Delta E_V = (\chi_2 - \chi_1) + E_{g2} - E_{g1} \dots \dots \dots 2.7$$

The total built in potential, V_d , is equal to the sum of partial built in voltages V_{d1} and V_{d2} , where V_{d1} and V_{d2} are the electrostatic potentials of the two semiconductors. Most of the thin film solar cells are based on heterojunctions. Carrier transport properties of heterojunctions are generally dominated by phenomena in the interface region. The current transport in the depletion

region is variously attributed to recombination, to tunneling or to combinations of tunneling and recombination involving energy levels at the surface. If $\Delta E_C > 0$ then a spike is formed in conduction band at the junction and for $\Delta E_C < 0$ a cliff in conduction band is formed. Usually the offset in conduction band is studied extensively in photovoltaic community as can it affect the flow of electron significantly.

2.2 Solar Cells

The solar cell can convert sunlight directly to electricity with good conversion efficiency. Therefore, it is already the leading source of energy in the space and also is an important candidate for alternative terrestrial energy. The solar cell efficiency depends on the spectral distribution of the radiation incident on the solar cell from the sun.

2.2.1 Solar Spectrum

The intensity of solar radiation in the free space at the average distance of earth from sun is defined as solar constant and has a value of 1353 W/m^2 . The degree to which atmosphere affects the solar spectrum received at earth is defined as air mass. Geometrical effects, varying path length through atmosphere described by air-mass AM_m .

$$m_r = \sec z,$$

where z is the angle of deviation from the normal incidence. Terrestrial sunlight varies greatly both in intensity and spectral composition. To allow meaningful comparison between the performance of different solar cells tested at different locations AM1.5 is used standard spectra (Figure 2.5).

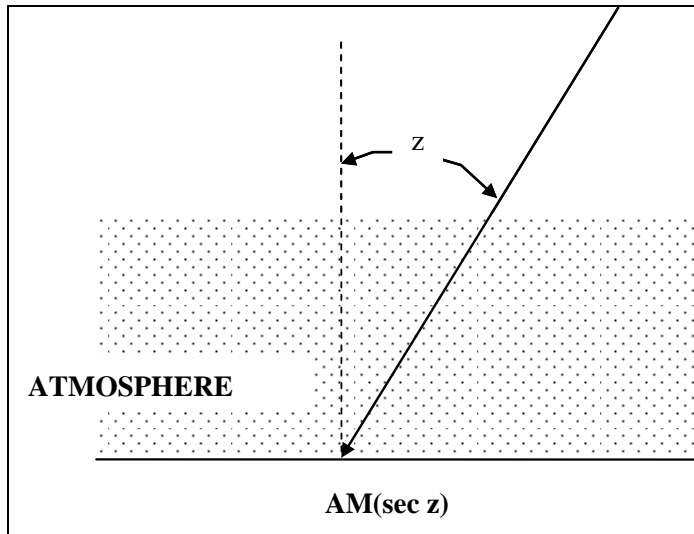


Figure 2.4: illustration of solar radiation spectrum AM_{m_r} . Where m_r stands for $\sec(z)$.

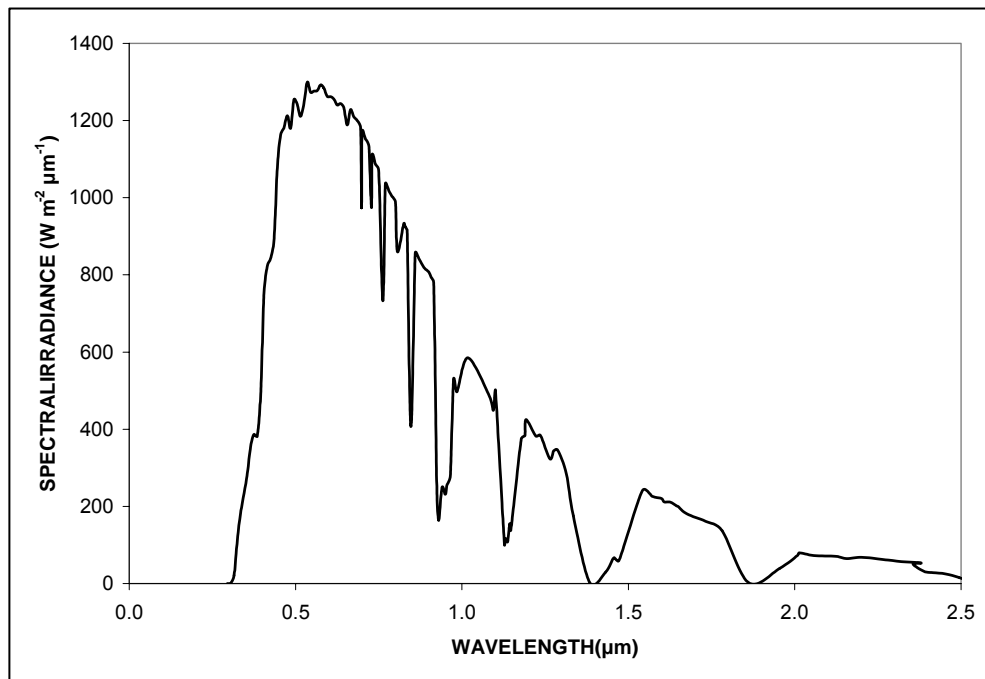


Figure 2.5: Standard AM1.5 solar spectrum.

2.2.2 *p-n Junction Solar Cells*

A typical solar cell is a diode that can be illuminated. When the solar cell is illuminated, photons with energies greater than the bandgap (E_g) can be absorbed. Photons with energy below

E_g are not absorbed and hence make no contribution to the cell output. Energy higher than E_g is usually converted to thermal energy. When the device is illuminated with photon having energies greater than the bandgap of absorber layer an electron-hole pair is created by excitation of electrons in the conduction band (process 1), leaving behind holes in valence band. The generated electrons can reach space-charge region (SCR) boundary, provided they do not recombine during diffusion process (process 2). The electrons which reach SCR boundary are swept across the space charge region assisted by the electric field (electric potential gradient) drift (process 3). Once electrons reach n-type layer they become majority carrier hence contributes to the external electric current. The generated electrons can recombine with holes. This can occur in the bulk (process 4) of film or at the interface of the p-n heterojunction (process 5).

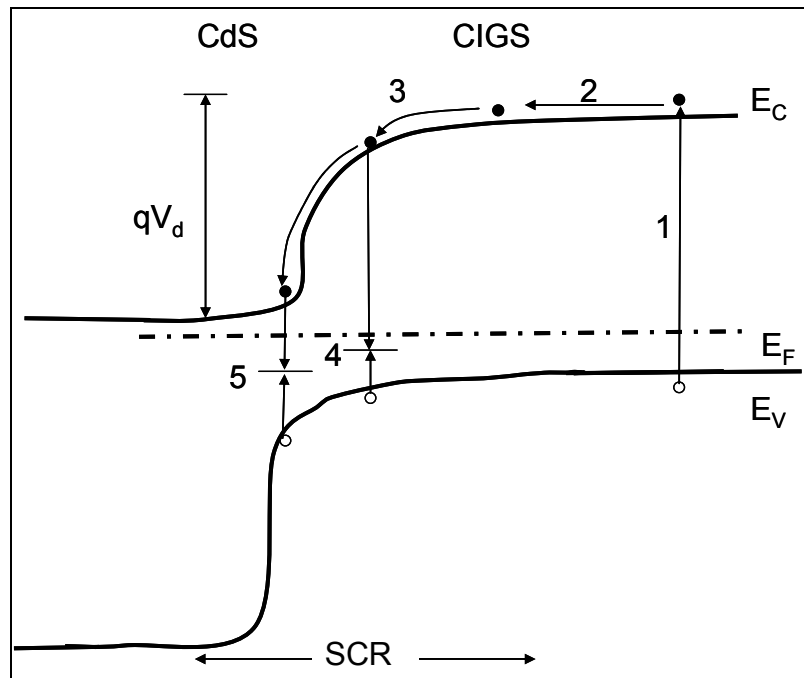


Figure 2.6: A typical band diagram of CIGS/CdS Solar cell

Ideal current-voltage (I-V) characteristic is shown in Figure 2.7

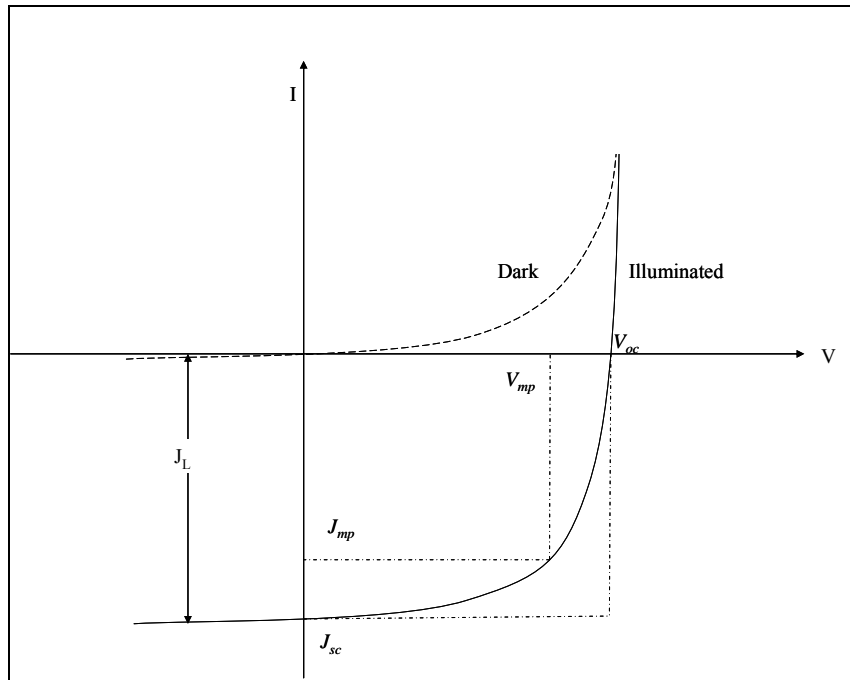


Figure 2.7: Ideal current-Voltage characteristics of a solar cell in the dark and under illumination.

The relationship between the current density, $J(V)$ with the applied bias voltage, V of a solar cell in the dark is given by the typical p-n junction diode equation given by

$$J(V) = J_0(e^{qV/AkT} - 1) \dots\dots\dots 2.8$$

where J_0 is the reverse saturation current density, q is the electron charge, A is the diode ideality factor, k is the Boltzmann constant, and T is the absolute temperature.

Under illumination a current J_L is generated, therefore overall current density equation becomes

$$J(V) = J_0(e^{qV/AkT} - 1) - J_L \dots\dots\dots 2.9$$

Equivalent circuit of a solar cell is shown in Figure 2.8 where I_L is light generated current, I_D is diode current, I_p is current through parallel resistance and $I = I_L - I_D - I_p$. Excitation of excess carriers due to illumination results in flow of photogenerated current. The photogenerated current is represented by a constant current source J_L is in parallel with the junction.

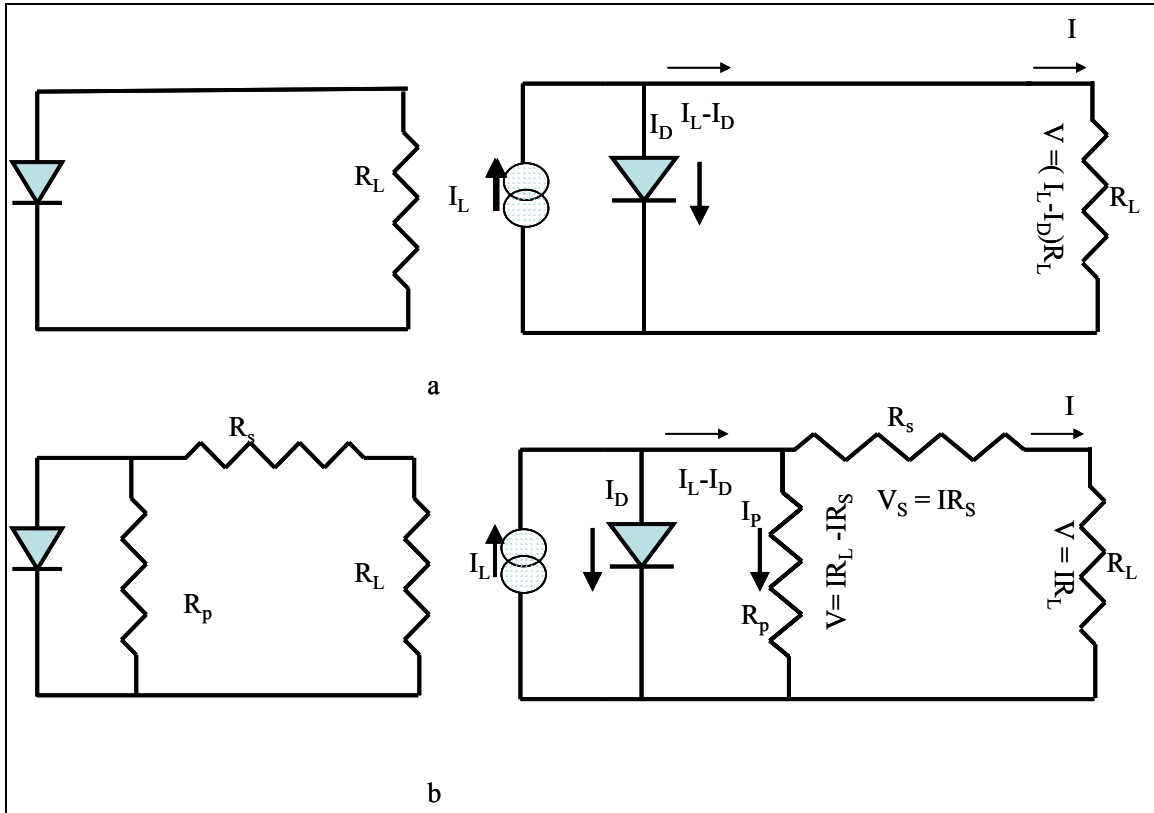


Figure 2.8: Equivalent circuit diagram for a solar cell (a) ideal solar cell in the dark and under illuminated condition (b) non-ideal solar cell with series and shunt resistance in the dark and under illuminated condition.

In non-ideal cells, series resistance, $R_s > 0$ and parallel resistance or shunt $R_p < \infty$ results in power losses. An equivalent circuit for such a cell is shown in Figure 2.8 (b) and a Current-

Voltage characteristic is shown in Figure 2.9, Figure 2.10. An increase in the series resistance does not affect the open circuit voltage, V_{oc} while the short circuit current, J_{sc} can be reduced with significant increase in the series resistance. Similarly, a reduction of shunt resistance does not affect J_{sc} , while significant reduction in the R_p affects V_{oc} considerably. Introduction of series and shunt resistance in the current equation of the ideal solar cell affects the fill factor as it changes the maximum power point.

The current density for non-ideal solar cells under illuminated condition is given by

$$[J(V) = J_0(e^{q(V-JR_s)/AKT} - 1) + (V - JR_s)/R_p - J_L] \dots\dots\dots 2.10$$

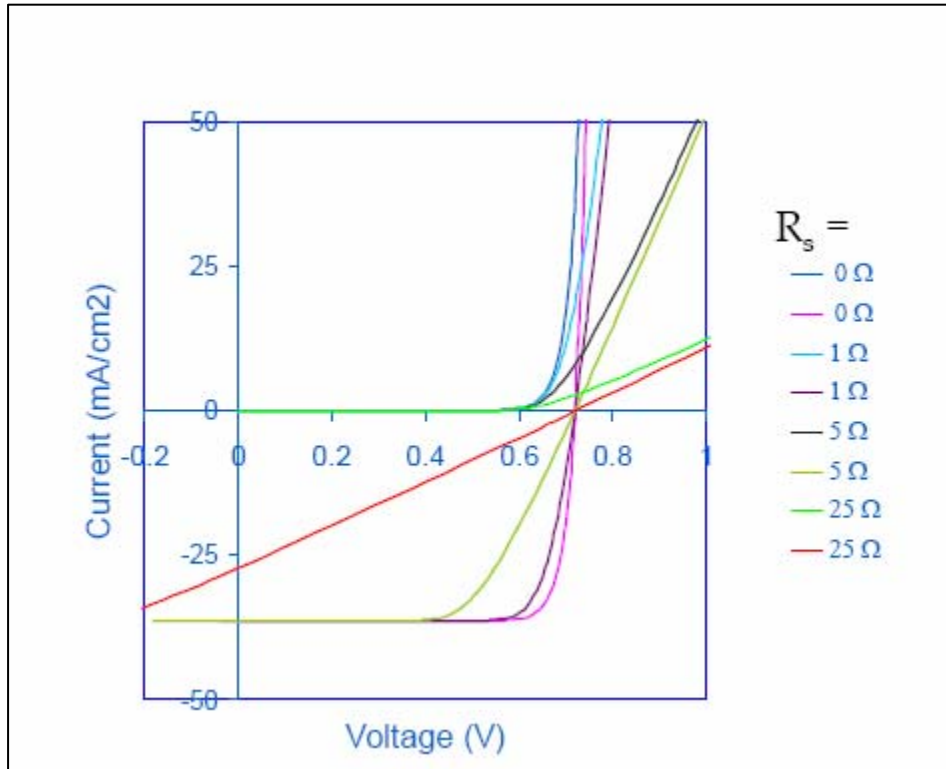


Figure 2.9: Effect of series resistance on short circuit current.

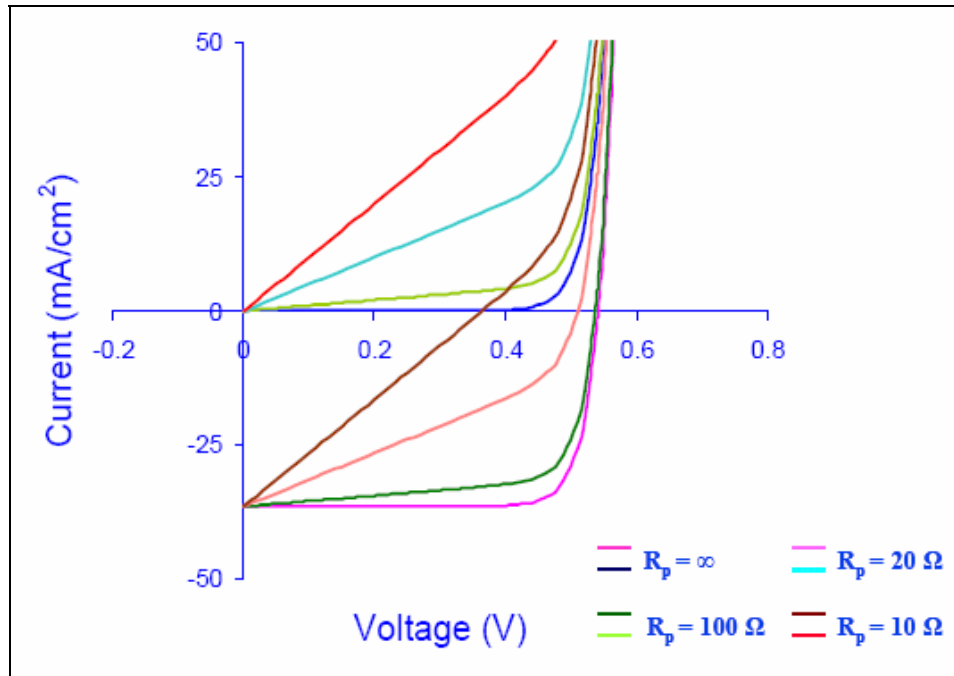


Figure 2.10: Effect of shunt resistance on open circuit voltage

Short circuit current (J_{SC}) is current is defined as current at zero bias,

$$J_{SC} = -J_L \dots \dots \dots 2.11$$

This relation holds only for ideal case. Open circuit voltage is obtained when current becomes zero.

$$V_{OC} = (AkT/q) \ln((J_L/J_0)+1) \approx (AkT/q) \ln (J_L/J_0) \dots \dots \dots 2.12$$

Fill factor is the measure of squareness of the J-V curve.

$$FF = V_{mp}J_{mp}/V_{OC}J_{SC} \dots \dots \dots 2.13$$

Where V_{mp} and J_{mp} are the voltage and current density corresponding to maximum power point on I-V curve.

Cell efficiency is given by

$$\eta = P_m / P_s = V_{OC}|J_{SC}|FF/P_s \dots \dots \dots 2.14$$

Where P_m is the maximum power and P_s is total solar input power.

2.2.3 Quantum efficiency

The quantum efficiency is defined as the number of electron-hole pair collected for each incident photon.

$$QE(\lambda) = C_{\text{collection carriers}} / N_{\text{incident photon}}(\lambda) \dots\dots\dots 2.15$$

One of the key factors that determine the quantum efficiency is absorption coefficient α . Since α is a function of wavelength, the wavelength range in which appreciable photocurrent can be generated is limited. The long wavelength cutoff (λ_c) is determined by the bandgap of absorber layer. For wavelength higher than λ_c the value of α is too low to allow band-to-band absorption. The short wavelength cutoff is determined by the least bandgap energy of among all window layers. Figure 2.11 shows various losses in a typical chalcopyrite solar cell.

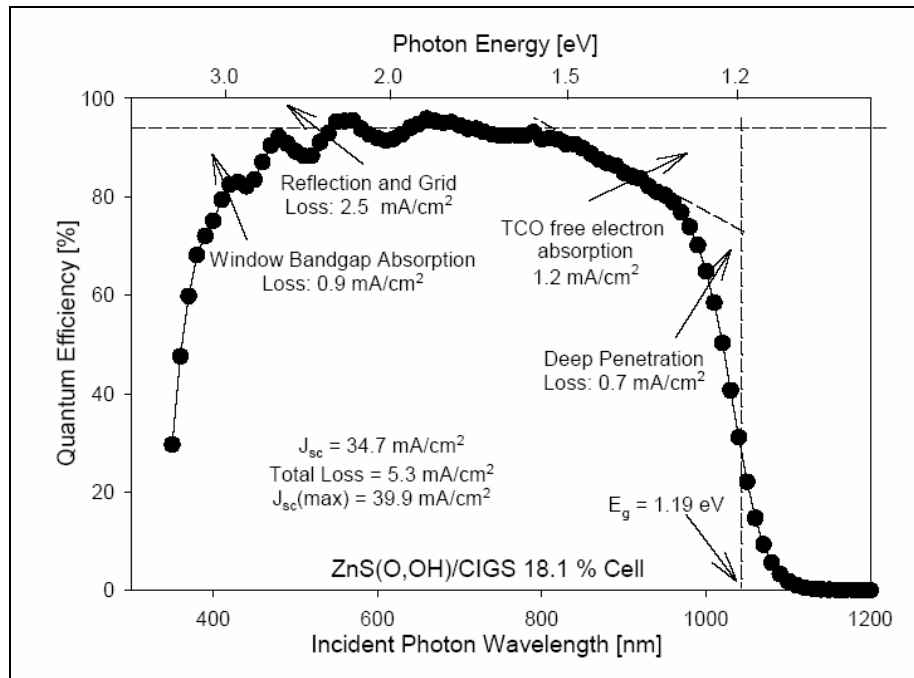


Figure 2.11: Quantum efficiency plot showing various losses in solar cell

3 CHALCOPYRITE SOLAR CELLS

Highly efficient I-III-VI₂ solar cells are fabricated with a multilayer structure as shown in Figure 3.1. The structure of the CIGS2 solar cells used for this work has a structure soda lime glass/Mo back contact layer/CIGS2/heterojunction partner/i-ZnO/ZnO:Al window bilayer/Ni/Al front contact grid. The inexpensive substrate and the fabrication techniques make the solar cells cost effective. The general process temperatures are approximately 500-550 °C.

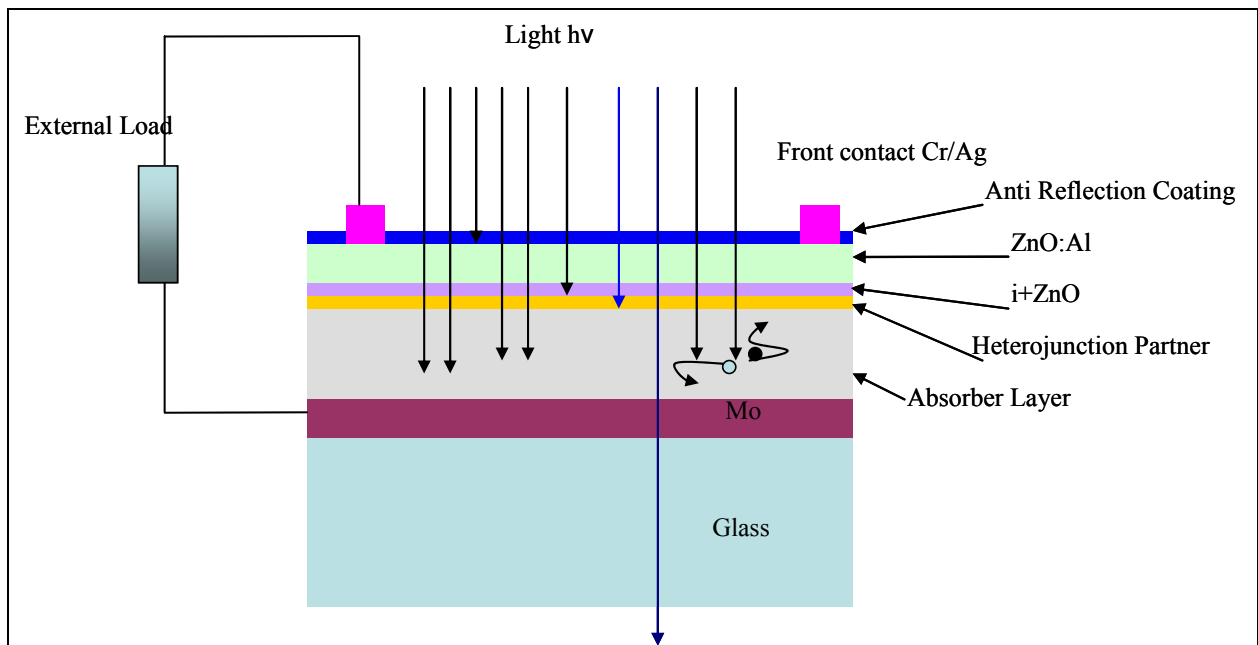


Figure 3.1: Schematic representation of the standard structure of the chalcopyrite solar cell

Soda lime glass is used as the substrate, as it is inexpensive and readily available. It has a softening temperature higher than the processing temperature for device formation. At higher processing temperatures, sodium diffuses through glass to the growing absorber layers, which can improve the film morphology and increase the conductivity of the film [3]. A thick (300-700

nm) Mo layer deposited by sputtering serves as back contact. Molybdenum forms a good ohmic contact and also can form MoS_2 which can improve adhesion.. A p-type absorber layer of copper indium gallium sulfide (CIGS₂) of thickness $\sim 2 \mu\text{m}$ is deposited on the Mo-back contact. Absorber layer can be prepared by co-evaporation process[4]-[6], spray pyrolysis [7] electrodeposition [8] [9] sulfurization [10]-[15] of metallic precursors (Cu, Ga, In) deposited by DC magnetron sputtering. CIGS₂ thin film absorber layer are usually grown in both Cu rich. All absorber layers used in this study are grown by sulfurization of metallic precursors Cu+Ga and In, in copper rich regime. CIGS₂ grown in copper excess composition forms Cu_{2-x}S quasi-liquid phase at the grain boundaries and on the surface of CIGS₂ thin film. Cu_{2-x}S is a quasi-liquid phase and acts as a flux during the growth of CIS₂ thin films [16]-[18]. Film grown in copper rich regime requires the removal of unavoidable secondary phase Cu_{2-x}S segregating at the surface by etching in a dilute KCN solution [15]. Etching leaves number of dangling bonds on the surface of absorber layer, which can act as recombination center for charge carriers. For passivating these dangling bonds, absorber layer is treated with a dilute solution of hydrogen peroxide and sulphuric acid. An n-type heterojunction partner is deposited by chemical bath deposition method. The window bilayer consists of 50 nm undoped i-ZnO and 500 nm of Al doped ZnO:Al transparent and conductive oxide, deposited by RF magnetron sputtering. ZnO is a wide bandgap material therefore; it allows most of the light spectra to be transmitted and has high conductivity. Ni/Al or Cr/Ag Front contact grid deposition by e-beam or thermal evaporation through a metal mask completes the cell.

3.1 Chalcopyrite absorber layer

One of the most important properties of I-III-VI₂ semiconductor family is that these are direct bandgap materials thus have high absorption coefficient. Therefore, these materials absorb light more efficiently (equation 3.1), so that a small thickness of few μm is adequate for absorption of most of the incident sunlight. The optical absorption coefficient is a function of energy of incident photon (Figure 3.2).

$$I(h\nu, x) = I(h\nu, 0)e^{-\alpha(h\nu)x} \dots\dots\dots 31$$

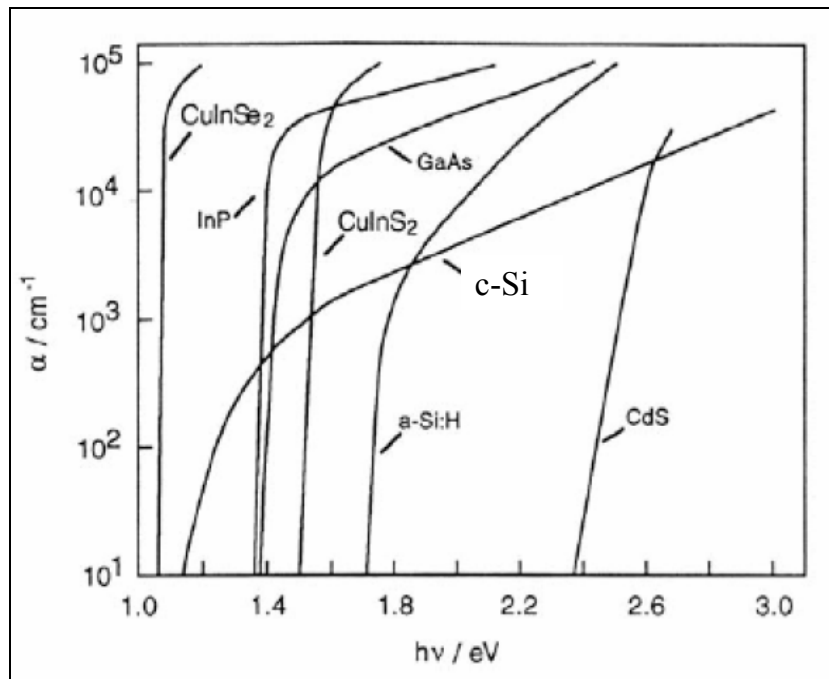


Figure 3.2 Dependence of the absorption coefficient on photon energy [19].

The typical absorption coefficient for CIS2 is in the range of 10⁵/cm for a photon energy of $h\nu = E_g + 0.2$ eV, where E_g is bandgap energy of respective material [20].

Copper indium sulfide, CIS2 and Copper Gallium Sulfide, CGS2 belong to I-III-VI₂ material family which crystallizes in tetragonal chalcopyrite structure. The chalcopyrite structure of CIS2 is similar to ZnS structure in which Zn atoms are replaced alternatively by Cu(I) and In(III) atoms. Each Cu and In atom has four bonds with S (VI) atom. In turn, each S atom has two bonds to Cu and two to In (Figure 3.3). Since the strength of the I-VI and III-VI bonds are in general different, the ratio of lattice constants c/a is not exactly 2. The quantity $2-c/a$ is a measure of the tetragonal distortion in chalcopyrites.

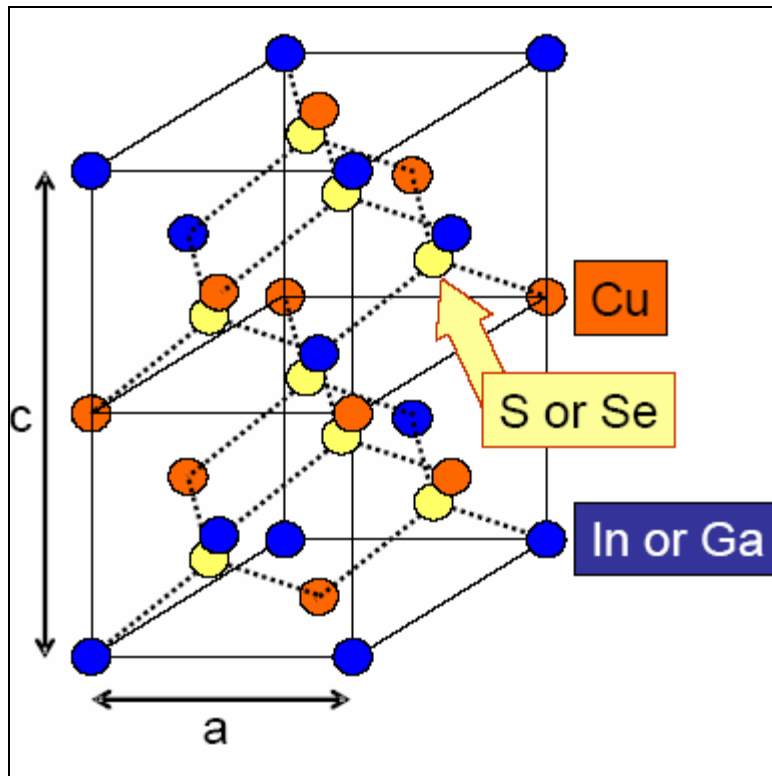


Figure 3.3: chalcopyrite structure [21]

For CIS2 the lattice parameters are $a=5.523 \text{ \AA}$ and $c=11.141 \text{ \AA}$ while for CuInS₂ the lattice $a=5.78 \text{ \AA}$ and $c= 11.62 \text{ \AA}$. Due to multitude of elements and compounds involved in

formation of I-III-VI₂ compounds the growth of films is extremely complex. The existence range of α phase CIS₂ in Cu₂S-In₂S₃ phase diagram at room temperature does not even include 25% stoichiometric content of copper. Therefore, there is a tendency of phase separation at room temperature. When CuInS₂ grown in copper rich regime, the excess Cu_{2-x}S quasi-liquid phase will segregate at the surface and grain boundaries.

3.2 Need and selection of heterojunction partners

In early stages of development of chalcopyrite solar cells, CdS layer deposited by evaporation was used as n-type heterojunction partner [22]. Owing to high resistivity and relatively lower bandgap (2.4 eV) of CdS layer, the solar cells had low values of fill factor and poor blue photon response. To circumvent these shortcomings CdS layer was partially replaced by ZnO layer which has higher band gap (~3.2 eV) [23]. Further improvements led to replace evaporated CdS with chemical bath deposited CdS layer [24][25]. Attempts to completely replace CdS and directly sputter deposit ZnO layer on absorber layer has not yet been successful.

The chemical bath deposited heterojunction partners can easily achieve surface passivation and junction formation. Even though p-n junction will form between n⁺ TCO's (transparent conducting oxides) and p-type absorbers, the quality of the junction is improved considerably with the introduction of an intermediate n-type layer(s). The advantages of using intermediate layers deposited by CBD are as follows:

As heterojunction partners used generally are highly resistive, they serve as intermediate layers that can prevent shunting between the TCO and the absorber.

These layers can protect the absorber surface from damage by high-energy ions during the n⁺ ZnO deposition by RF-sputtering

The chemical constituents of buffer material passivate surface defects and/or dope the near-surface layer of the absorber layer.

The selection criteria for heterojunction partner is listed below:

To form a good junction partner with a p-type CIGS absorber, a buffer material should be n-type.

Heterojunction partner layers with optimum resistivity are required to reduce the possibility of shunting of a junction without excessively increasing the series resistance.

Lattice parameters for heterojunction partner layer must be as close as possible with those of the absorber layer to reduce lattice mismatch hence also the interfacial recombination velocity.

Band gap of heterojunction partners need to be sufficiently wide (>3.2 eV), to avoid blue photon absorption in this layer.

Another important heterojunction-material selection criterion is its electron affinity, which will determine discontinuities in the energy bands at the buffer/absorber interfaces.

Solar spectrum above energy 3.2 eV is absorbed in window layer (ZnO, $E_g=3.2$ eV) however it results in a photocurrent loss of less than 1 mA/cm². CdS ($E_g = 2.4$ eV), however, can lower the photocurrent through absorption by up to six mA/cm² by absorbing available solar spectrum above 2.4 eV. By making the CdS buffer layer thinner, the absorption losses are reduced. Thus, part of the short-wavelength current loss is recovered. However, heterojunction partners with bandgap above 3.2 eV will nearly eliminate these absorption losses.

3.3 Heterojunction materials used in I-III-VI₂ Solar cells

II-VI compounds such as CdS, ZnS, CdSe, ZnSe and ternary $Zn_xCd_{1-x}S$ etc are widely used as heterojunction partners for chalcopyrite solar cells, II-VI semiconductor materials can

crystallize in either the cubic zinc-blende (sphalerite) (Figure 3.4) (beta) phase or the hexagonal wurzite (alpha) phase (Figure 3.5).

Zinc-blende structure: Interpenetrating face-centered cubic sublattices of Zn and S are separated by a vector $a/4 [111]$. Each cation (anion) atom is tetrahedrally coordinated with four anions (cations). Alternatively, the structure can be described as an f.c.c. anion sublattice with alternate tetrahedral sites occupied by cations (Figure 3.4). The distance between nearest neighbor is $\sqrt{3}a/4$. The stacking of the ZnS/CdS dimers along the $\langle 111 \rangle$ direction is ABCABC. Bonding in Zinc blende structure is a mix of covalent (sp^3 hybrids) and ionic bonding, the degree of which depends on the difference in electronegativity between the anion and the cation. Number of broken bonds per unit area is lowest on (111) surface, and higher on (001) and (110). On the other hand, the electrostatic energy is the lowest on (110) surface. Therefore, (110) Surface is the most stable lowest energy, surface for the zincblende structure.

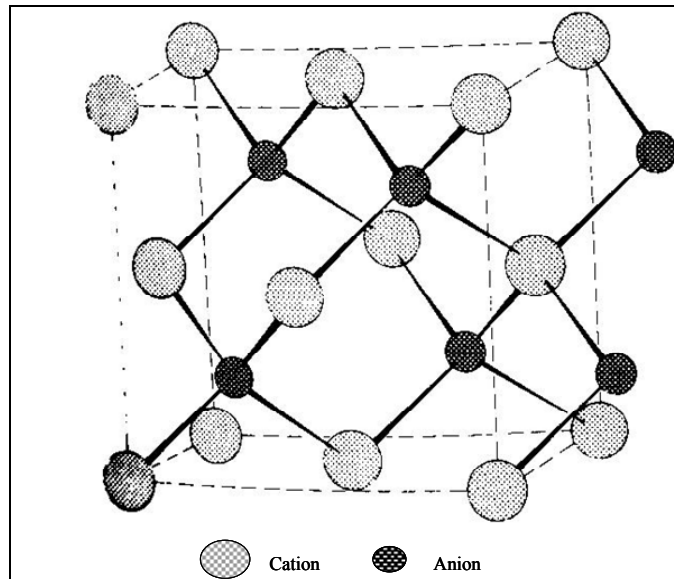


Figure 3.4: Zinc blende structure

Wurtzite structure: In the wurtzite structure, the S or the Zn atoms form a hcp array, with half of the tetrahedral sites occupied by another kind of atoms. Bonding is a mix of sp^3 covalent bonds and ionic bonds due to the large electronegativity difference. Thin films of wurtzite compounds tend to grow with strong [0001] texture. The tetrahedrons in wurtzite all are oriented in one direction and produce the hexagonal (six fold rotational) symmetry. The structure of wurtzite phase can be represented by stacking layers of tetrahedrons using a sequence of ABAB.

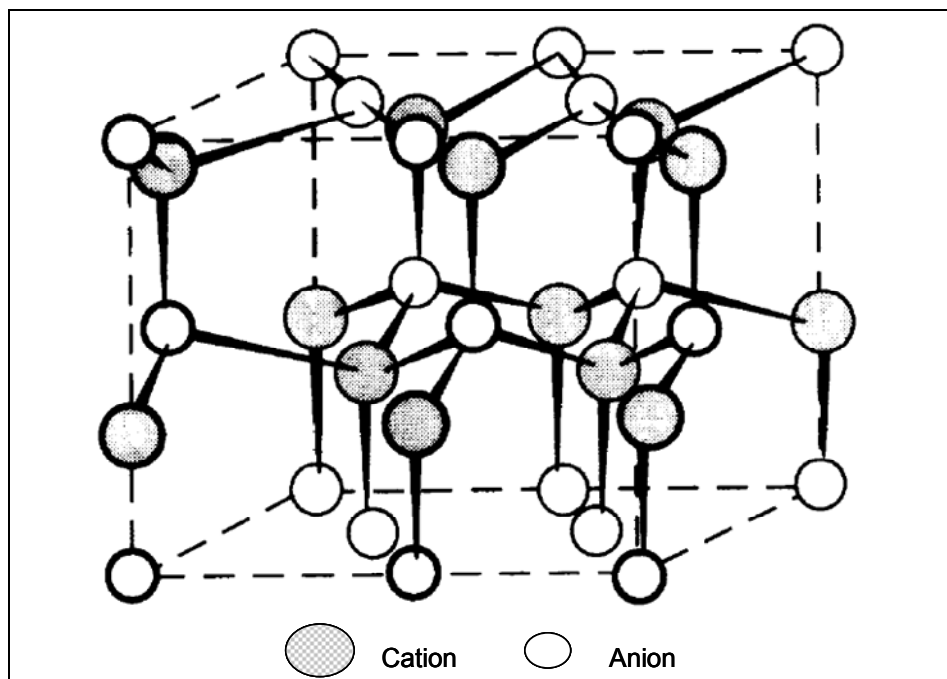


Figure 3.5: Wurtzite structure

Table I: Various properties of ZnS and CdS at 300K [26]

Property / Material	ZnS	CdS
Zinc Blende Lattice Parameter a_0 at 300 °K	0.541 nm	0.582 nm
Zinc Blende Nearest-Neighbor Dist. at 300 °K	0.234 nm	0.252 nm
Zinc Blende Density at 300 °K	4.11 g.cm ⁻³	4.87 g.cm ⁻³
Wurtzite Lattice Parameters at 300 °K		
a_0	0.3811 nm	0.4135 nm
c_0	0.6234 nm	0.6749 nm
c_0/a_0	1.636	1.632
Wurtzite Density at 300 °K	3.98 g.cm ⁻³	4.82 g.cm ⁻³
Phase Stable at 300 °K	Zinc blende & wurtzite (both occur in nature)	Wurtzite
Melting Point	1850 °C wurtzite, 150 atm	1750 °C wurtzite, 100 atm
Refractive Index zinc-blende structure	2.368	
Refractive Index wurtzite structure	2.356, 2.378	2.506, 2.529
Energy Gap E_g zinc blende structure	3.68 eV, Direct	2.50 eV, Direct
Energy Gap E_g wurtzite structure	3.911 eV, Direct	2.50 eV, Direct

3.4 Cadmium sulfide

CdS is the most widely used heterojunction partner for I-III-VI₂ solar cells. A record efficiency of 19.5% has been obtained on CIGS solar cells with CdS heterojunction layer deposited by chemical bath [26] <http://www.semiconductors.co.uk/propiiivi5410.htm>

[27]. Though high efficiencies have been achieved with CIGS absorber layer using CdS as heterojunction partner same has not been achieved for CIGS2/CIGSeS solar cells.

A fundamental limit on the efficiency of the CdS/ I-III-VI₂ cell is the low value of the bandgap of the CdS window layer. A current loss of 6 mA/cm² for AM1.5 global spectrum at 100 mW/cm² equivalent intensity results as a consequence of high absorption in CdS heterojunction layer owing to its lower band gap (~2.4 eV) (Figure 3.6). This loss can be overcome by using higher bandgap energy materials as heterojunction partners for CIGS2 solar cells.

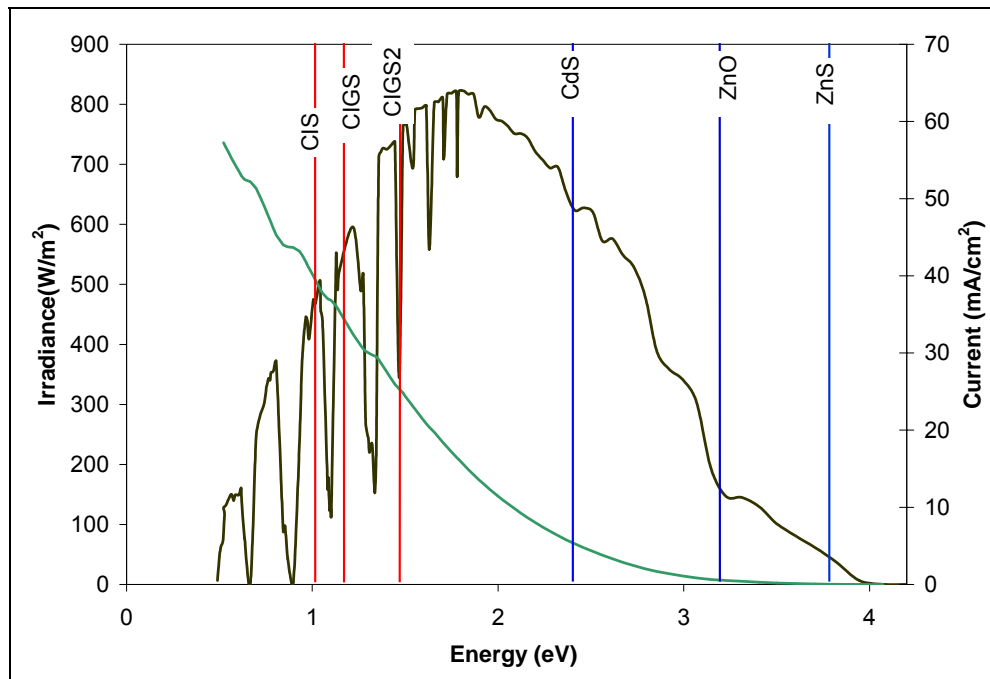


Figure 3.6: AM1.5 Solar Spectrum and maximum attainable short circuit current density with various band gap energies.

Another consideration for heterojunction formation is band offset. A condition near of perfect match without the formation of either a spike or a cliff is achieved in high efficiency CIGS solar cells with CdS a heterojunction partner because the difference in the bandgap values is compensated by the difference between the electron affinities [28]. While a cliff in conduction band is postulated when the conduction band minimum for CIGS2 lies above the conduction band minimum of CdS [28][29]. This leads to reduced open circuit voltage and higher interface dominant recombination [30] [31]. A conduction band offset of $-0.45 (\pm 0.15)$ eV and a valence band offset) of $-1.06 (\pm 0.15)$ eV was obtained for CIGS2/CdS junction in earlier studies at the Florida Solar Energy Center as shown in Figure 3.7. Optimum conduction band matching can be achieved if heterojunction partners with higher electron affinities i.e. higher conduction band position are utilized with absorbers having optimized In/(In+Ga) ratio. As the conduction band energy position of CIGS2 is a function of In/ (In+Ga) ratio.

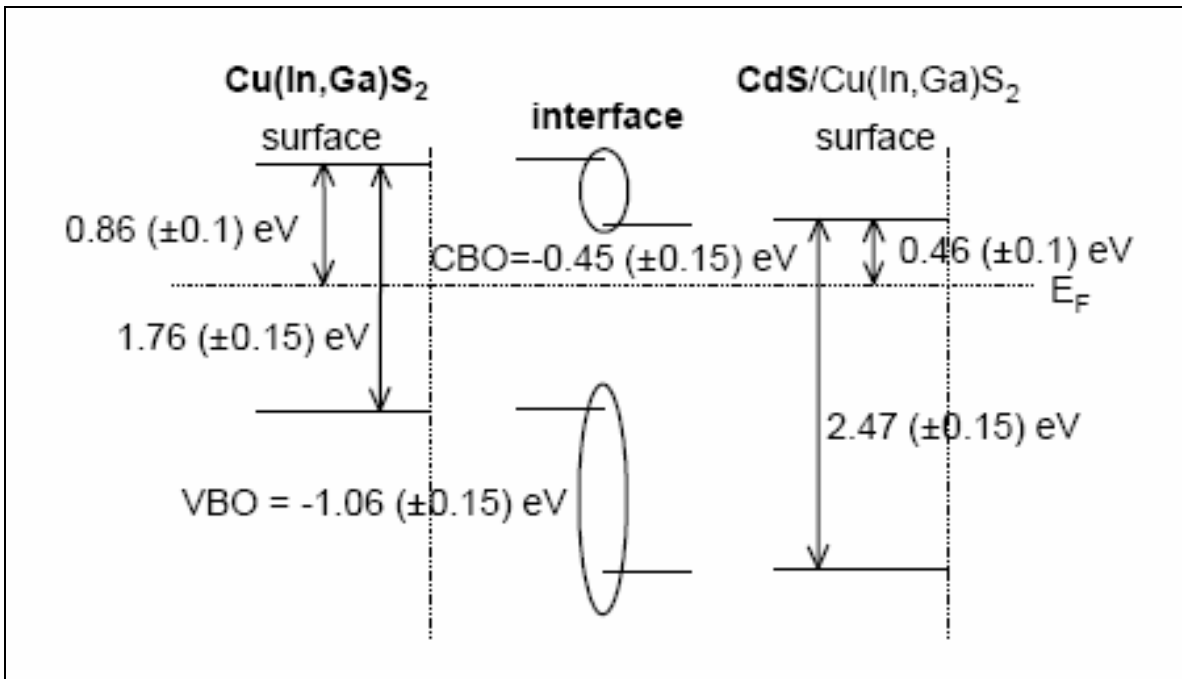


Figure 3.7 Schematic band diagram for CIGS₂/CdS interface [29]

Another consideration is lattice mismatch in CIGS2/CdS solar cells. In case of $\text{CuIn}_{1-x}\text{Ga}_x\text{Se}_2$ (lattice parameter $\sim 5.8 \text{ \AA}$, when $x = 0$) CdS (lattice parameter $\sim 5.8 \text{ \AA}$) has a better lattice match. However same is not true for $\text{CuIn}_{1-x}\text{Ga}_x\text{S}_2$ (lattice parameter $\sim 5.5 \text{ \AA}$, when $x = 0$)/CIGSeS as absorber layers. The difference in lattice constant between the heterojunction components results in a periodic array of dangling bonds. The edge dislocations ideally form a regular net at the interface leading to current paths that decrease V_{OC} and fill factor.

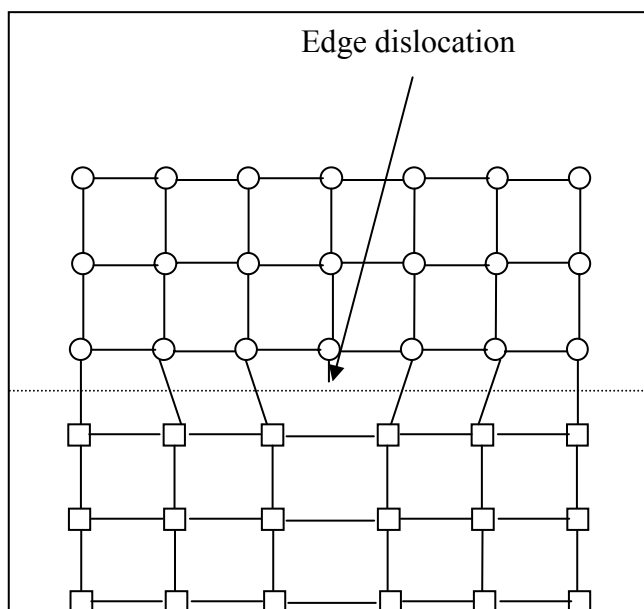


Figure 3.8 Schematic diagram of the interface of two single crystal with different lattice parameters, resulting in formation of edge dislocation.

3.5 Zinc sulfide

ZnS with wide band gap energy (3.8eV) is an attractive heterojunction partner because it is transparent to almost the complete solar spectrum (Figure 3.6). ZnS as heterojunction partner has shown better blue photon response resulting in higher short circuit current ZnS as heterojunction partner has also shown a high conduction band offset (spike) with CIGS absorber

layer [32]. CIGS thin film solar cells with ZnS as the heterojunction partner have achieved efficiencies comparable to those achieved by CIGS thin film solar cells with CdS as the heterojunction partner [32]-[34].

3.6 Zinc cadmium sulfide

Utilization of $Zn_xCd_{1-x}S$ as heterojunction partner can improve the performance of chalcopyrite solar cells due to an increase in the photo-generated current. The optical bandgap of $Zn_{1-x}Cd_xS$ varies between bandgap values of ZnS and CdS [35]. Increased blue photon transparency results in higher current.

Another important consideration is decrease in electron affinity with increasing Zn content in the film which can shift the position of conduction band higher. Thus, the conduction band alignment can be engineered by varying composition of $Zn_{1-x}Cd_xS$ films.

The lattice constant of $Zn_{1-x}Cd_xS$ unit cell is dependant on the composition of the $Zn_{1-x}Cd_xS$ films. There is considerable disagreement in the literature over the variation of lattice constants with respect to composition for $Zn_{1-x}Cd_xS$ [35]-[40], most of the publications reporting a negative variation from the linearity. However, the varying composition of film can minimize the lattice mismatch between absorber layer and heterojunction partner. Therefore, the density of dangling bonds (dislocations) can be reduced leading to better V_{OC} and fill factors.

3.7 Chemical bath deposition technique

In the present work, heterojunction layer deposition has been carried out using chemical bath deposition (CBD). Several techniques such as thermal evaporation, spray pyrolysis, molecular beam epitaxy, sputtering, chemical bath deposition, close space sublimation, and laser

ablation have been used to produce II-VI thin films. Among these, CBD method (Figure 4.1) is most commonly used because it is simple, and economically reproducible technique. It can be applied in large area deposition at low temperatures. CBD technique is based on the controlled release of metal ion (M^{2+}) and sulphide (S^{2-}) ions in an aqueous bath in which the substrates are immersed. In this process, release of metal ion (M^{2+}) is controlled by using a suitable complexing agent. The deposition begins with nucleation followed by growth in which the thickness of film increases with duration up to the terminal phase.

4 EXPERIMENTAL TECHNIQUE

4.1 Chemical Bath Deposition Technique:

Aqueous solution of NH_4OH , CdSO_4 , ZnSO_4 and $\text{NH}_2(\text{CS})\text{NH}_2$ were added to an organic solvent in suitable concentration. Initially aqueous solution of ZnSO_4 , CdSO_4 , and NH_4OH were mixed in a organic solvent. The temperature of solution increased to approximately 80°C and aqueous solution of $\text{SC}(\text{NH})_2$ is added. At this stage the samples were introduced in the solution. The bath was maintained at 80°C with constant stirring. The deposition was carried out until inception of homogenous reaction indicated by increasing turbidity of the solution. All glass samples were ultrasonically cleaned with deionized water prior to deposition and also the samples were washed in ultrasonic bath after each deposition. The Figure 4.1 shows an experimental setup for chemical bath deposition.

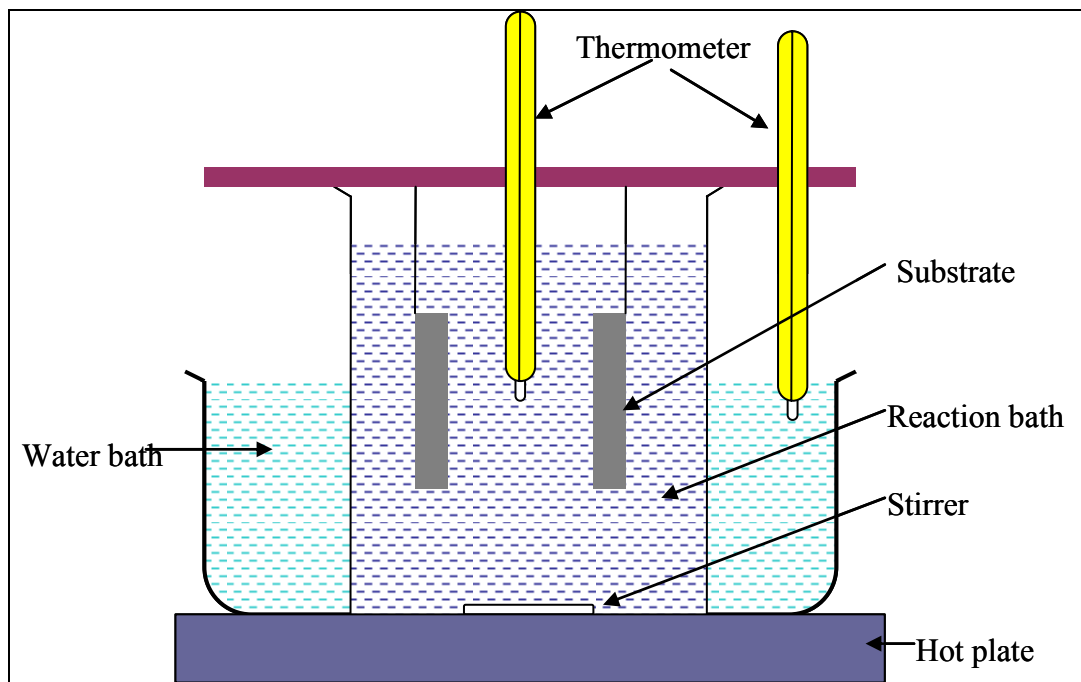
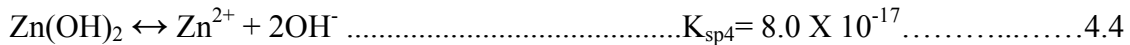
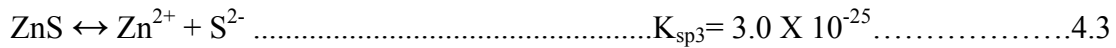
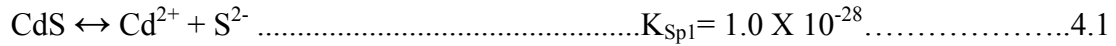


Figure 4.1: Experimental setup for chemical bath deposition

4.2 Chemistry of Bath

Chemistry of Zinc and cadmium are same in many aspects so it might be expected that deposition of their chalcogenides is also similar. However, there is a significant difference in their chalcogenide formation tendency. This difference is caused by the large solubility product difference for various compound formations.



The tendency of zinc ions to form hydroxides is almost two orders of magnitude higher as compared to that of cadmium ions as can be calculated by solubility products of Zn(OH)_2 and Cd(OH)_2 . Whereas sulfide formation tendency is lower for zinc ion. Therefore, for ZnS deposition it is important to have lower pH values as compared to CdS deposition. However, if too low pH value is maintained, the very slow rates for hydrolysis of thiourea limit the reaction rates.

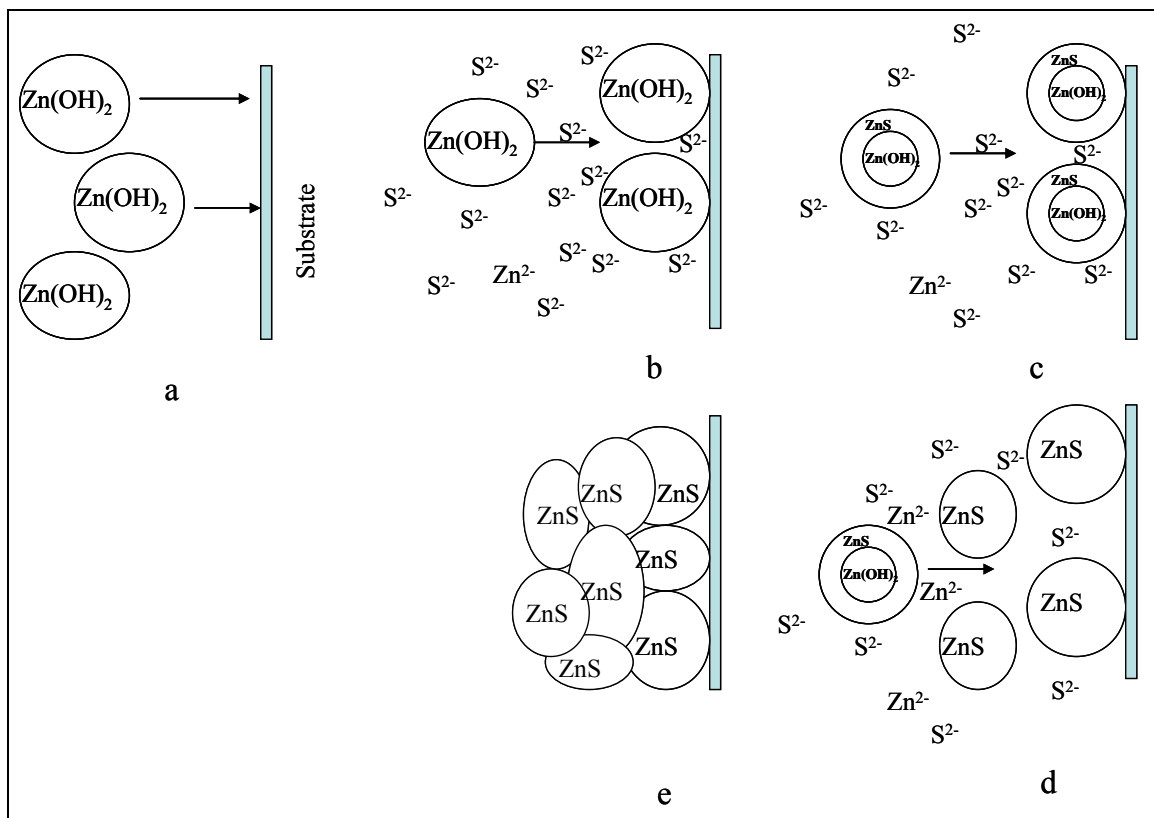


Figure 4.2: Schematic diagram showing various stages in cluster mechanism for Zinc sulfide growth

As discussed in last paragraph, in an alkaline solution CdS deposition is preferred over ZnS. For $\text{Zn}_x\text{Cd}_{1-x}\text{S}$ deposition free Cd^{2+} concentration must be much lower than free Zn^{2+} concentration in the solution in order to deposit ZnS according to simple solubility product considerations. The strength of complexation (with NH_4OH) is almost comparable, therefore it is possible to adjust the complexant concentration such that there is no Cd(OH)_2 present in the solution. In that case, CdS deposition occurs by ion-to-ion mechanism, while ZnS deposition occurs by cluster mechanism.

5 RESULTS AND DISCUSSIONS

The aim of this research work was to develop an alternative heterojunction partner layer, and study the effects of deposition parameters on the device performance. In the first phase the depositions were carried out on commercial chemical vapor phase deposited SnO₂:F coated glass. As the surface of SnO₂:F is not very smooth, it provided nucleation sites for deposition (similar to actual deposition condition). Zn_xCd_{1-x}S depositions were carried out in a mixture of organic solvent and aqueous solution of ZnSO₄ (0.02 M), CdSO₄ (0.0002 M), SC(NH)₂ (0.25M) and NH₄OH (0.58 M) in a chemical bath [41]. The solution temperature was maintained at approximately 80°C. Homogenous nucleation was observed to occur after 15 minutes of deposition under these conditions, hence multiple depositions each lasting 15-minutes were carried out so as to achieve build higher thicknesses.

Auger Electron Spectroscopy (AES) was carried out for Zn_xCd_{1-x}S film deposited in three depositions (Figure 5.1). Surface analysis showed the presence of Zn, Cd, S on the surface. Carbon was observed in all the films and it is speculated that the organic solvent might be the source of this carbon. Moreover, carbon was observed in the depth of the film in lower concentrations. This indicates that carbon was also derived from the atmosphere at the surface.

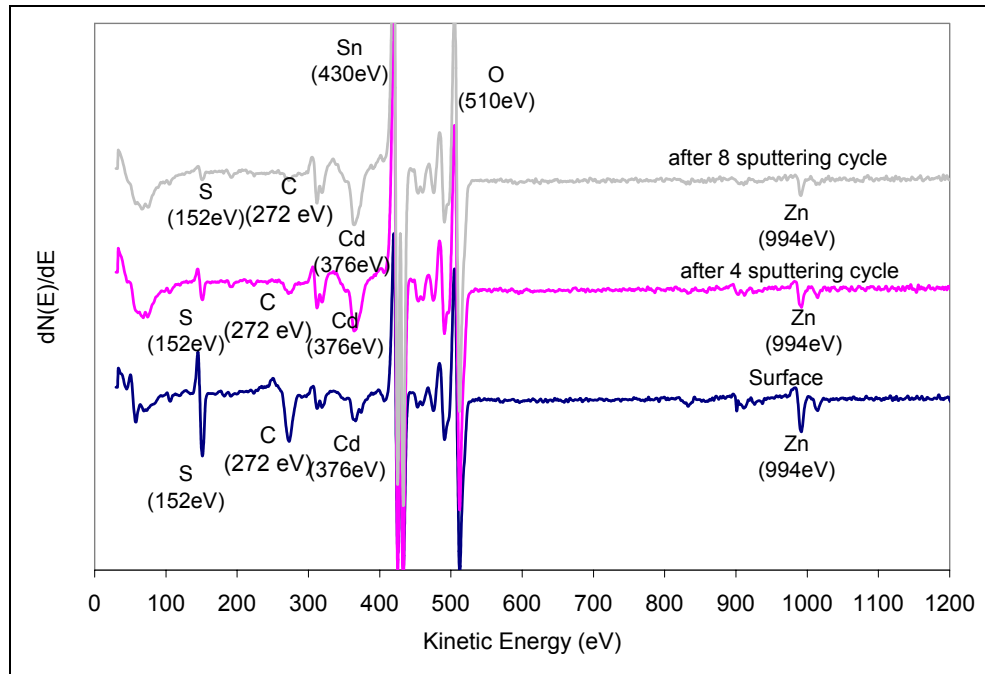


Figure 5.1: Differential Auger spectra of $Zn_xCd_{1-x}S$ thin film deposited on $SnO_2:F$ glass

5.1 Effects of variation of deposition parameters on device performance

CIGS2 absorber layer was prepared by sulfurization of CuGa-In metallic precursors deposited by DC magnetron sputtering. Mo-coated sodalime glass was used as the substrate. An approximately 2- μ m thick absorber layer was grown in the copper-rich regime. The substrate was then subjected to etching using dilute KCN solution. The heterojunction partner was then deposited on the CIGS2 absorber using chemical bath deposition. The CIGS2 absorber used for various set of experiments was not the same. However, for any one set of experiment absorbers from same batch, i.e. fixed Cu/(In+Ga) ratios were used. Moreover, for studying effect of various deposition parameters, a standard composition [41] of reagents was used as reference to study the effect of variation of deposition parameters.

Table II: Standard concentrations used for studying effects of various compounds used in CBD parameters

Compound	Concentration
ZnSO ₄	0.02 M
CdSO ₄	0.0002 M
(NH ₂) ₂ CS	0.25 M
NH ₄ OH	0.58 M

5.1.1 Influence of deposition time

Multiple depositions each of 15 minutes duration were carried out to procure thicker films. The deposited films were ultrasonically cleaned after each deposition. The optical transmission spectra in wavelength range of 300 to 1100 nm were measured using a ultra-violet to visible UV-VIS Recording Spectrophotometer. Figure 5.2 shows optical transmittance spectra with varying deposition time. Thinner Zn_xCd_{1-x}S films (i.e. with lower deposition time) show more than 90% transmittance for long and short wavelengths, while films with higher deposition time shows more than 80% transmittance for longer wavelengths (above 600nm). The film with lower deposition time has a higher transmittance, which can result in higher short circuit currents. On the other hand, thicker films will provide better coverage of the absorber layer in the solar device and also minimize the damages caused during subsequent deposition of window layer by sputtering.

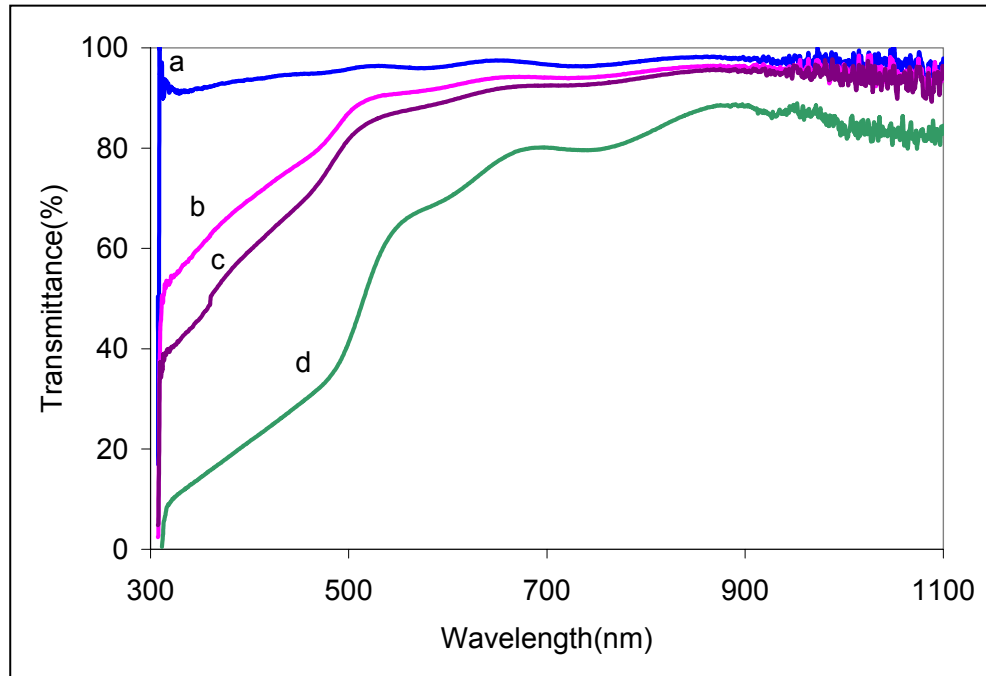


Figure 5.2: Optical transmittance spectra for (a) $Zn_xCd_{1-x}S$ thin film deposited in a single 15 minute run (b) $Zn_xCd_{1-x}S$ layer prepared in two 15 minute depositions (c) $Zn_xCd_{1-x}S$ layer deposited in three 15 minute runs (d) standard CdS layer deposited on $SnO_2:F$ glass.

Figure 5.3 shows J-V characteristics of completed cells with CIGS2 absorber layer for various deposition times of $Zn_xCd_{1-x}S$ and standard CdS heterojunction layer. Cells with $Zn_xCd_{1-x}S$ as heterojunction partner have shown higher short circuit current density as compared to the cells with CdS. This can be attributed to better blue photon response due to higher bandgap of $Zn_xCd_{1-x}S$ as compared to CdS as heterojunction partner. The highest fill factor and best cell efficiency of 4.9% was obtained for $Zn_xCd_{1-x}S$ thin film deposited in two 15-minute CBD runs. Higher shunt resistances were obtained solar cells prepared using ZnCdS layer deposited in three 15-minute runs. However, the series resistance also increased. Therefore, 30 minutes of

deposition time was found to be near optimum deposition time. A linear interpolation of data showed that 32 minutes of deposition should provide maximum device efficiency.

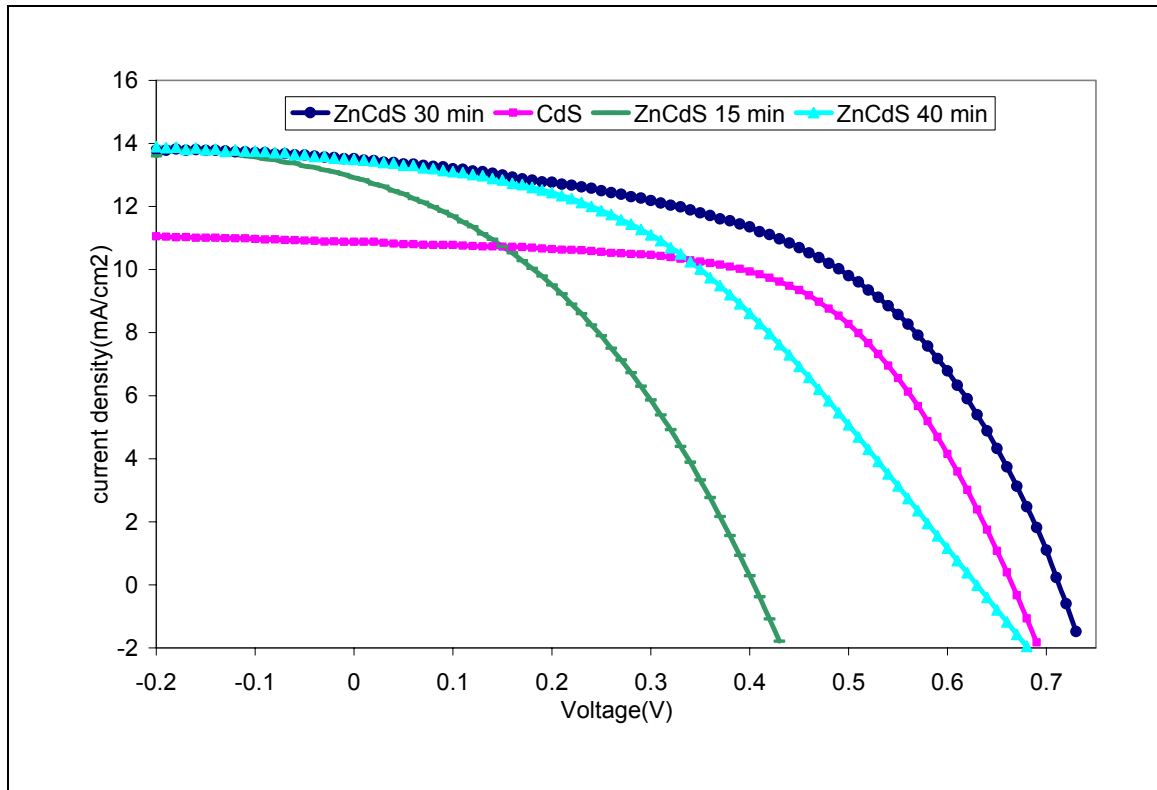


Figure 5.3 The J-V characteristics for CIGS₂/Zn_xCd_{1-x}S solar cells using ZnCdS layers having total deposition times of 15, 30 and 40 minutes respectively and CIGS₂/CdS solar cells under AM 1.5 condition measured at FSEC.

X-ray diffraction (XRD) pattern of Zn_xCd_{1-x}S deposited for 30 minutes on SnO₂:F coated glass showed only broad peaks indicating amorphous nature of the deposited film (Figure 5.4).

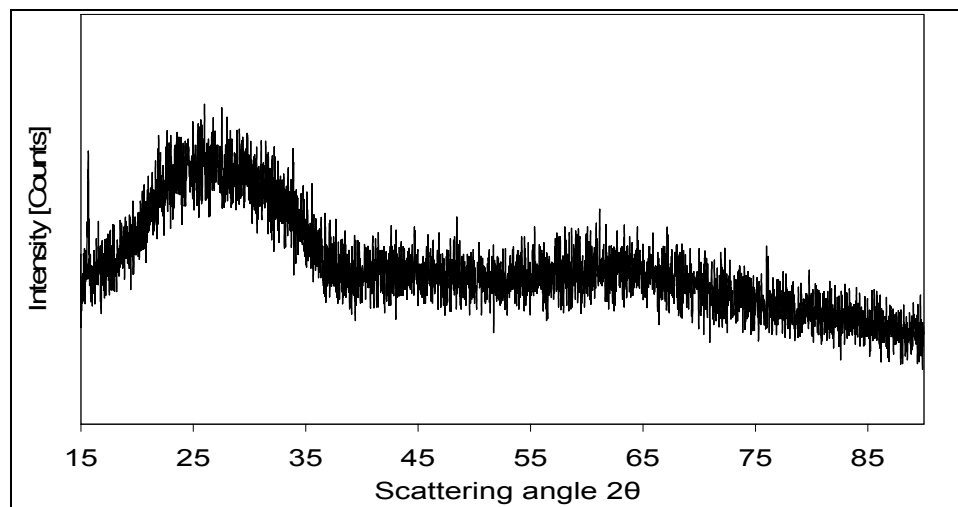


Figure 5.4: X-ray diffraction pattern of $Zn_xCd_{1-x}S$ film deposited on tin oxide coated glass substrate.

The near surface composition of ZnS and $Zn_xCd_{1-x}S$ films deposited for 30 minutes on CIGS2 samples was characterized by X-ray photoelectron spectroscopy (XPS) studies carried out using Physical Electronics 5400 ESCA equipped with $Mg K_{\alpha}$ X-ray source. The XPS spectra are shown in Figure 5.5 and Figure 5.6.

The measured XPS spectra were shifted to match carbon peak to the binding energy of 284.6 eV in order to eliminate the charging effects. Cadmium, zinc, sulfur, oxygen and carbon were identified in the deposited film. Carbon was initially present for all films deposited by CBD process. XPS spectra of CBD $Zn_xCd_{1-x}S$ layers showed peaks of $Cd 3d_{5/2}$, $Zn2P_{3/2}$, and $S2P_{3/2}$ at approximately 405.1 eV, 1022.5 eV and 161.4 eV respectively [42]. Peaks of CdS (405.3 eV), CdO_2 (404 eV) and $Cd(OH)_2$ (405 eV) were indicated by $Cd3d_{5/2}$ core level spectra while the peaks of ZnS , and ZnO eV were indicated by $Zn2p_{3/2}$ core level spectra. $Zn2P_{3/2}$ and $S2P_{3/2}$ peaks were observed in the case of ZnS layers.

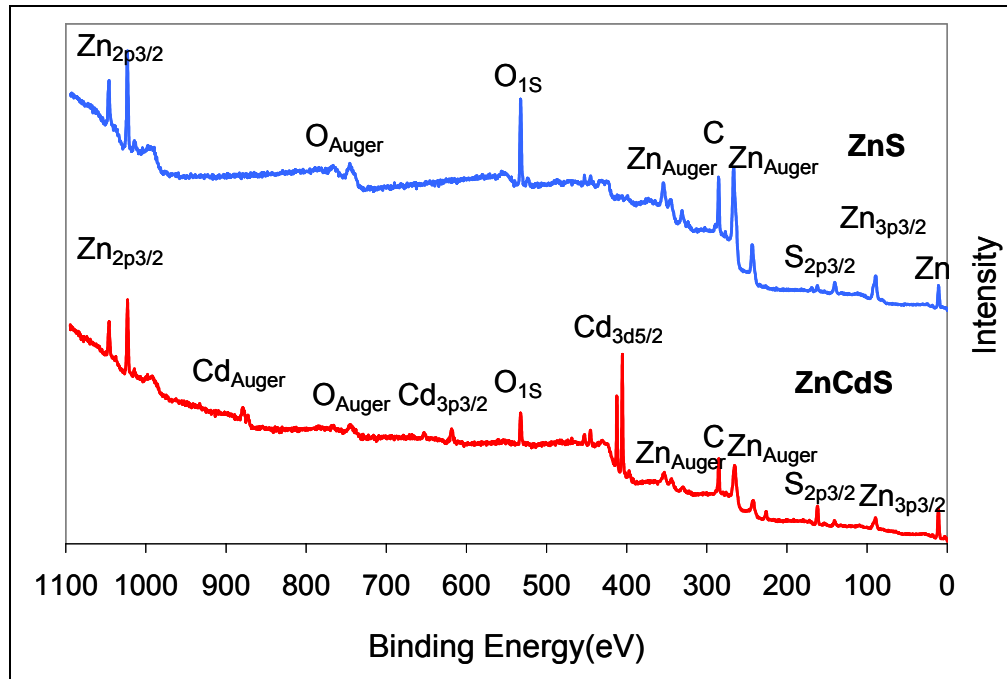


Figure 5.5: XPS spectra for ZnS and $Zn_xCd_{1-x}S$ thin films deposited on CIGS2 film.

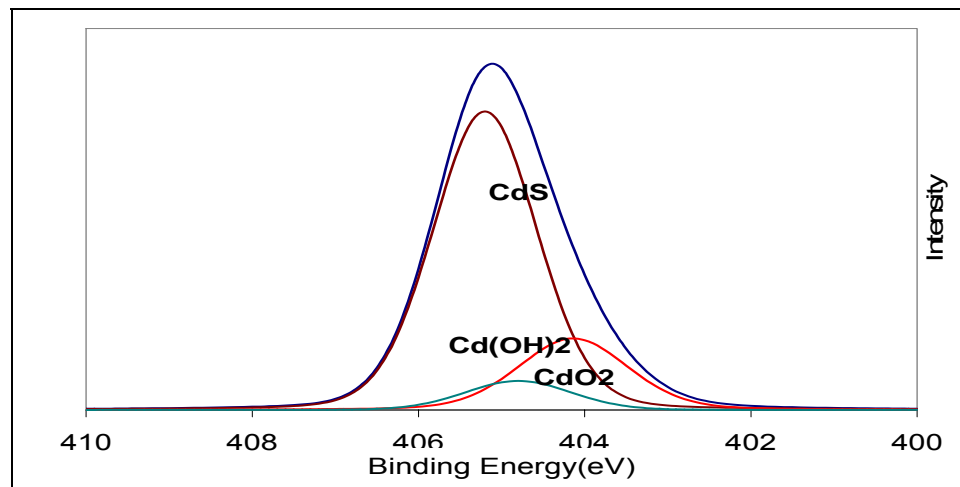


Figure 5.6: Cd $3d_{5/2}$ peak in the XPS spectrum of a $Zn_xCd_{1-x}S$ layer. Curve fitting to show contribution of CdS, $Cd(OH)_2$ and CdO_2 peaks to corresponding XPS peak is also plotted.

5.1.2 Influence of ammonium hydroxide concentration

Experiments were carried out to understand the effect of varying NH_4OH concentration and the corresponding pH variation. Various $\text{Zn}_x\text{Cd}_{1-x}\text{S}$ films were deposited with 0.09 M, 0.027 M, 0.58 M and 1.2 M NH_4OH . The NH_4OH concentrations were selected so as to maintain the pH of the bath at 9.5, 10.5, 11, and 11.5 respectively. Concentrations of the other chemicals were kept same as the standard solution. Two depositions were carried out at 80°C for 15 minutes. Open circuit voltage and short circuit current variation is shown in Figure 5.7. Fill factor of 60 and above was obtained at 0.09M NH_4OH concentration corresponding the bath pH of 9.5 indicating good quality of the film. A high shunt resistance and low series resistance which are the desired criteria for good quality solar cells, were obtained for film grown at the same NH_4OH concentration. SEM micrographs (Figure 5.8, Figure 5.9a) show that crystallinity of films grown at pH values corresponding to lower NH_4OH concentrations is higher as compared to that of film deposited with higher NH_4OH concentrations. This explains the higher series resistance at higher NH_4OH concentrations used in chemical bath depositions due to reduction in crystallinity. Therefore, for high quality solar cells, a very low concentration of NH_4OH and thus corresponding low pH of 9-9.5 is required for chemical bath deposition of $\text{Zn}_x\text{Cd}_{1-x}\text{S}$.

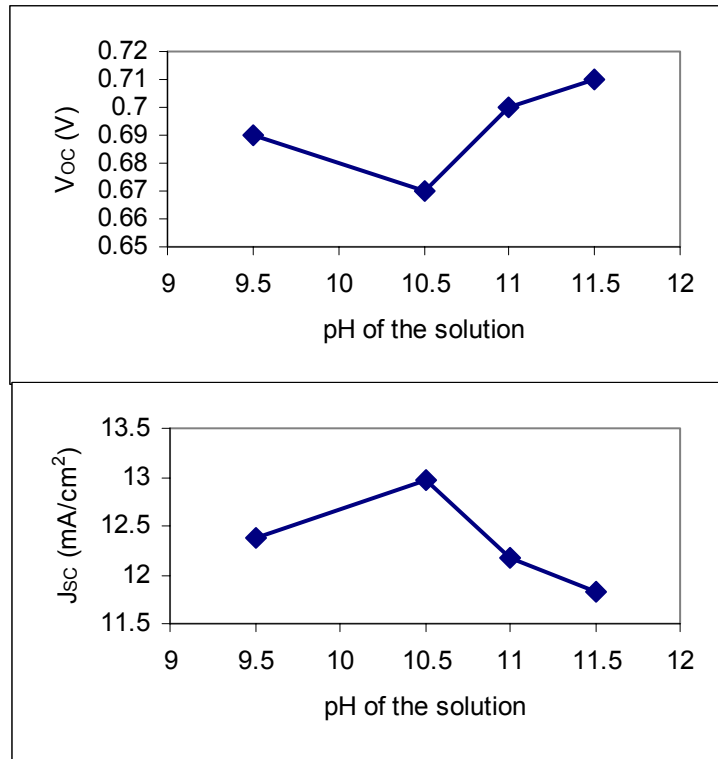


Figure 5.7: Open circuit voltage and short circuit current density values for various pH of bath controlled by NH₄OH concentrations

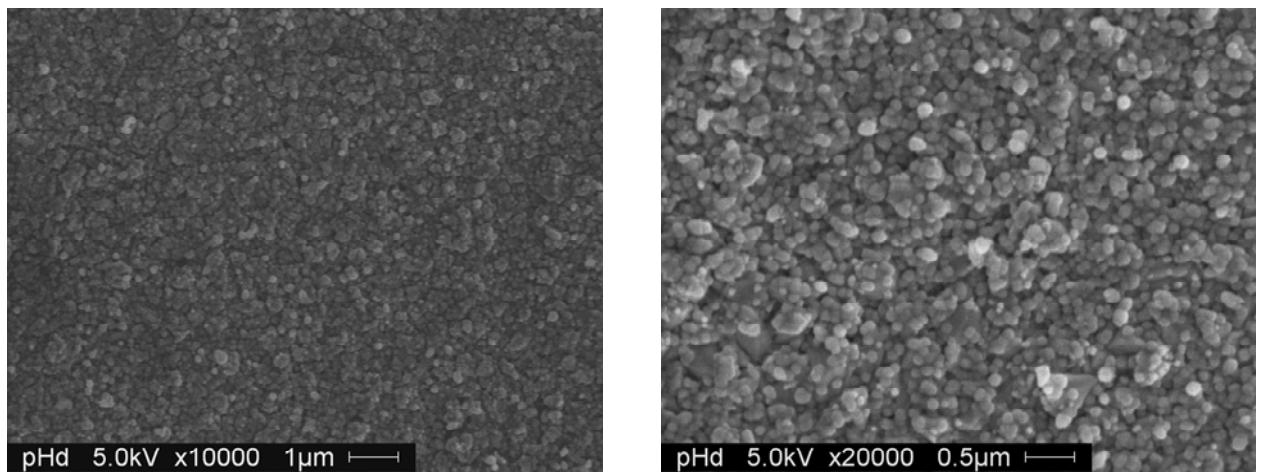


Figure 5.8: SEM micrographs for of the surface of Zn_xCd_{1-x}S film deposited on SnO₂:F glass, with NH₄OH concentration of 0.09 M during chemical bath deposition.

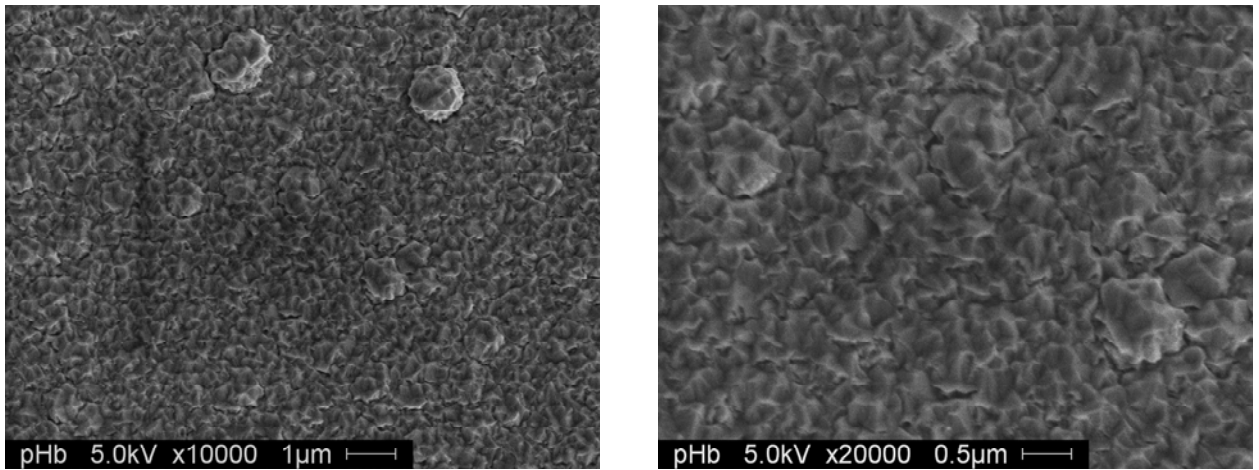


Figure 5.9: SEM micrographs of the surface of $Zn_xCd_{1-x}S$ film deposited on $SnO_2:F$ glass, with NH_4OH concentration of 0.027M during chemical bath deposition.

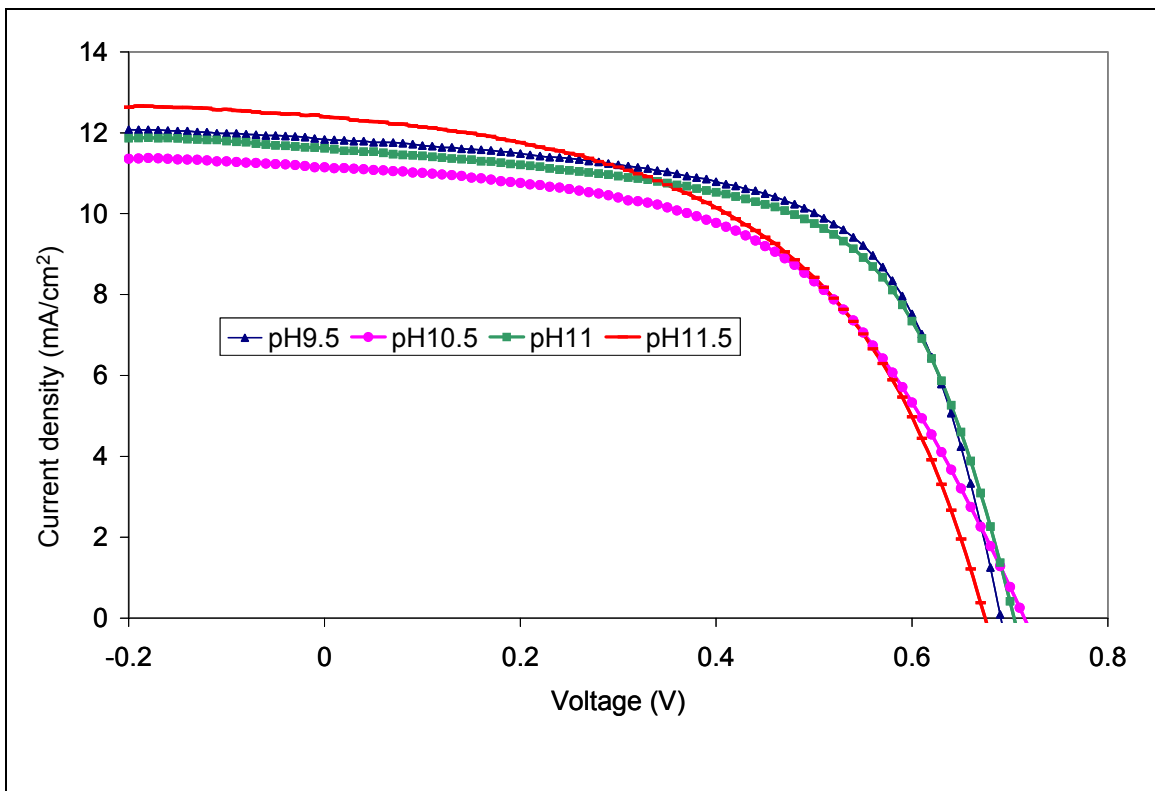


Figure 5.10 The J-V characteristics taken at FSEC for CIGS2/ $Zn_xCd_{1-x}S$ prepared at various values of pH of bath adjusted using NH_4OH concentration.

5.1.3 Effect of cadmium sulfate concentration.

Concentration of cadmium sulfate, CdSO_4 was varied from 0.0001 M to 0.0003 M keeping the other deposition parameters same as the standard parameters. Increasing concentration of CdSO_4 leads to decrease in transmittance of light through the film as shown in Figure 5.11. This effect may be attributed to lower bandgap obtained with increasing cadmium concentration in the film. SEM Micrographs of films deposited with higher concentrations of CdSO_4 during the chemical bath depositions are shown in Figure 5.12 and Figure 5.13, they seem to reveal better crystallinity and compact grains. Current-Voltage (I-V) characteristics (Figure 5.14) indicate that layer deposited with 0.0003 M CdSO_4 concentration has higher fill factors indicating good junction properties. As the grains are compact for higher CdSO_4 concentration, there are fewer shunt paths leading to improved shunt resistance. Series resistance is lower which indicates that near optimum thickness of $\text{Zn}_x\text{Cd}_{1-x}\text{S}$ layer is obtained for this composition. However, the J_{SC} and V_{OC} values obtained for 0.0003M CdSO_4 concentration were lower as compared to corresponding values obtained for CdSO_4 concentration of 0.0002 M and 0.0004 M. Therefore, fine-tuning of CdSO_4 concentration in 0.0003M range might result in optimum device properties. I-V curve also indicates that ZnS(O,OH) film grown without CdSO_4 led to inferior quality cells.

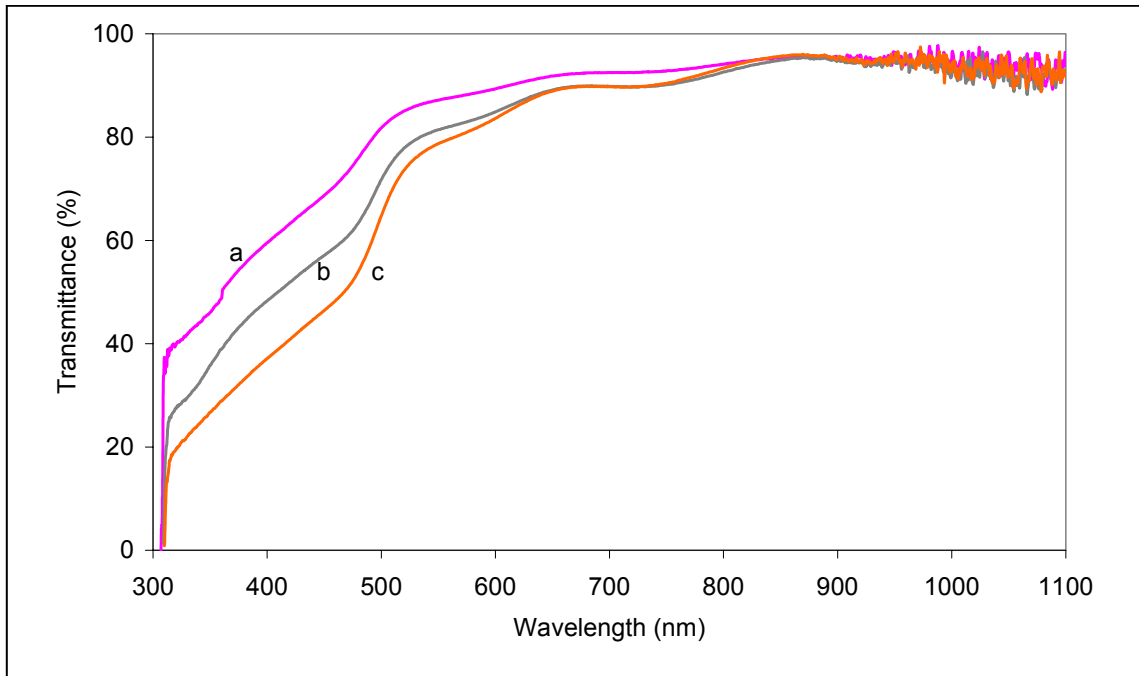


Figure 5.11: Optical transmittance spectra for $Zn_xCd_{1-x}S$ films for varying $CdSO_4$ concentration, (a) 0.0001M (b) 0.0002M (c) 0.0004M

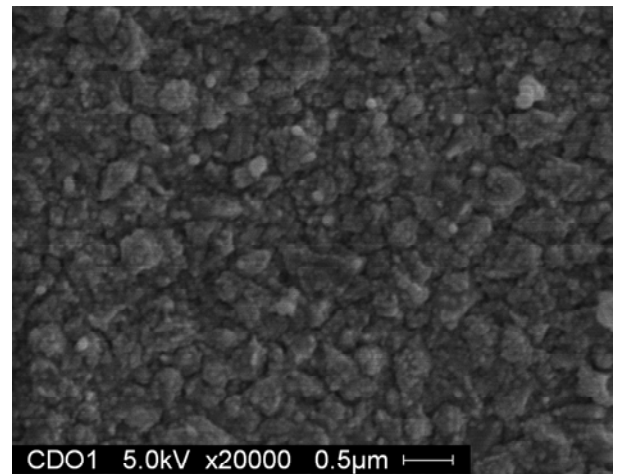
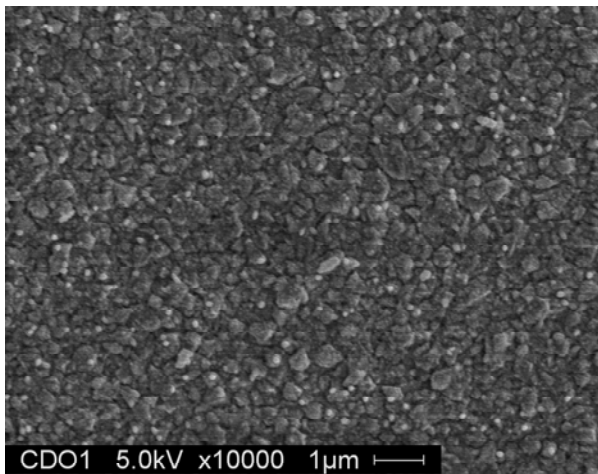


Figure 5.12: SEM micrographs for of the surface of $Zn_xCd_{1-x}S$ film deposited on $SnO_2:F$ glass, for $CdSO_4$ concentration of 0.0001M during chemical bath deposition.

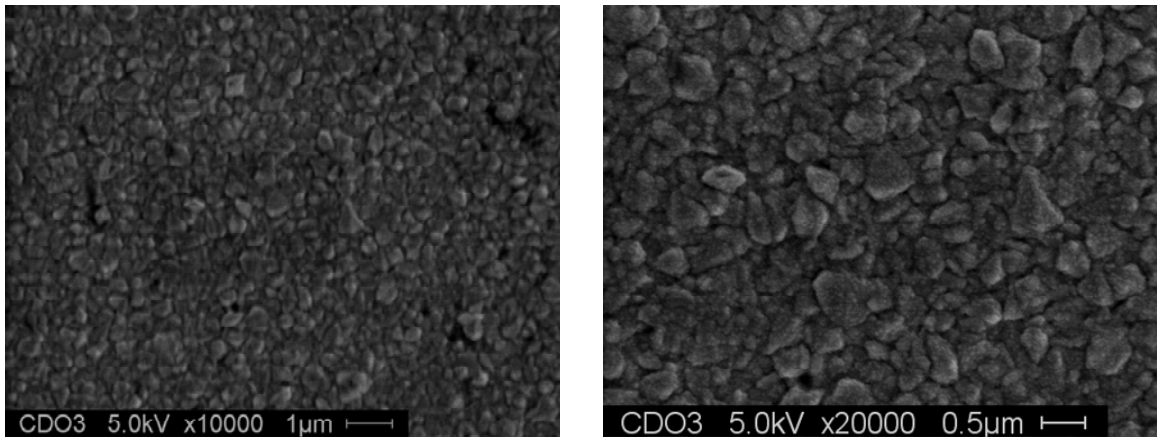


Figure 5.13: SEM micrographs for of the surface of $Zn_xCd_{1-x}S$ film deposited on $SnO_2:F$ glass, for $CdSO_4$ concentration of 0.0003M during chemical bath deposition.

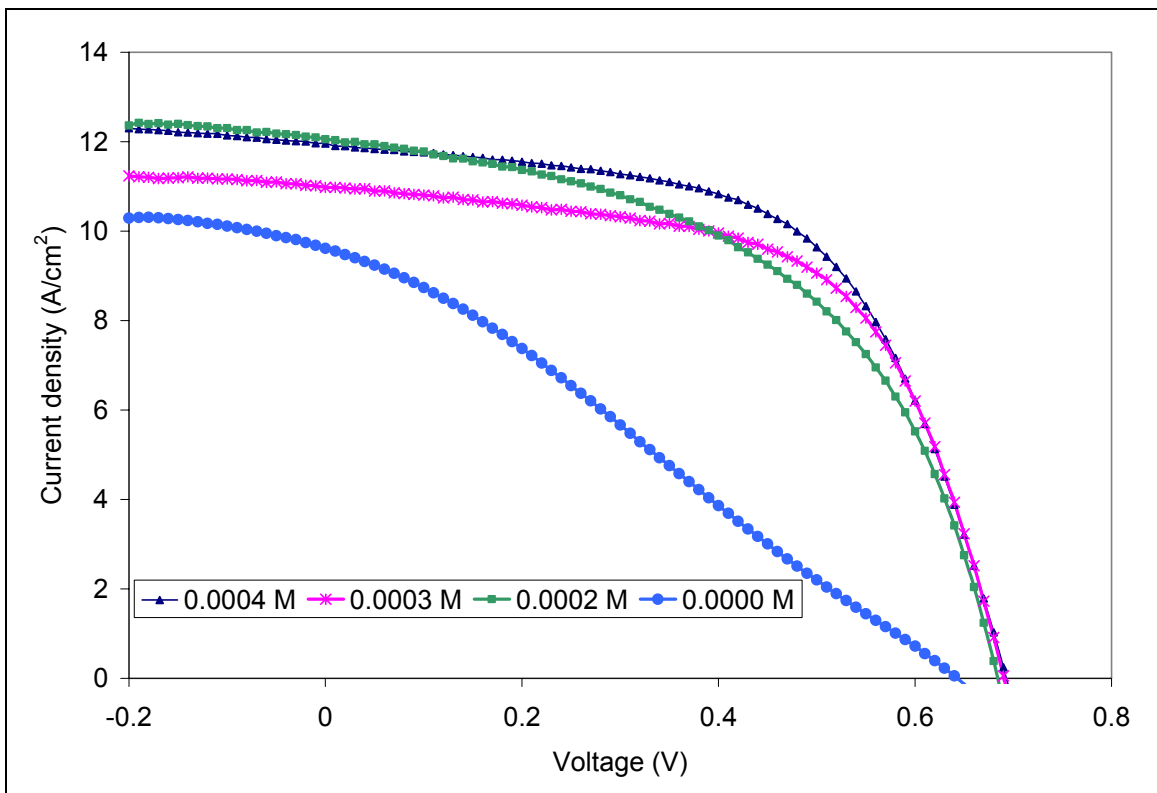


Figure 5.14: The J-V characteristics taken at FSEC for CIGS2/ $Zn_xCd_{1-x}S$ device deposited with various $CdSO_4$ concentrations.

5.1.4 Zinc sulfate concentration variation

The transparency of the heterojunction layer increased with increasing concentration of ZnSO_4 in solution in chemical deposition bath as shown in Figure 5.15. This effect can be attributed to higher zinc sulfide concentration in deposited films at higher concentrations of ZnSO_4 in the chemical bath which leads to bandgap widening thus higher transmittance. SEM micrograph in Figure 5.16 indicates better crystallinity at higher ZnSO_4 concentration in the chemical bath. Higher short circuit current with lower open circuit voltage values were obtained for concentrations of 0.01 M ZnSO_4 . Slightly lower short circuit current and higher open circuit voltage values are obtained with concentrations of 0.004 M ZnSO_4 in chemical deposition (Figure 5.17). The reasons for lower J_{SC} values with increasing Zn content is probably due to unfavorable band alignment between heterojunction partner and absorber layer as the conduction band shifts up with increasing Zinc content in the film. Higher efficiency and better Fill factor values were obtained for concentrations of 0.001 M ZnSO_4 in chemical bath. The shunt resistance ($\sim 1000 \Omega$) for all devices with varying ZnSO_4 concentration remained almost constant, indicating that the deposition rate is either independent or a very weak function of ZnSO_4 concentration used for the chemical bath deposition.

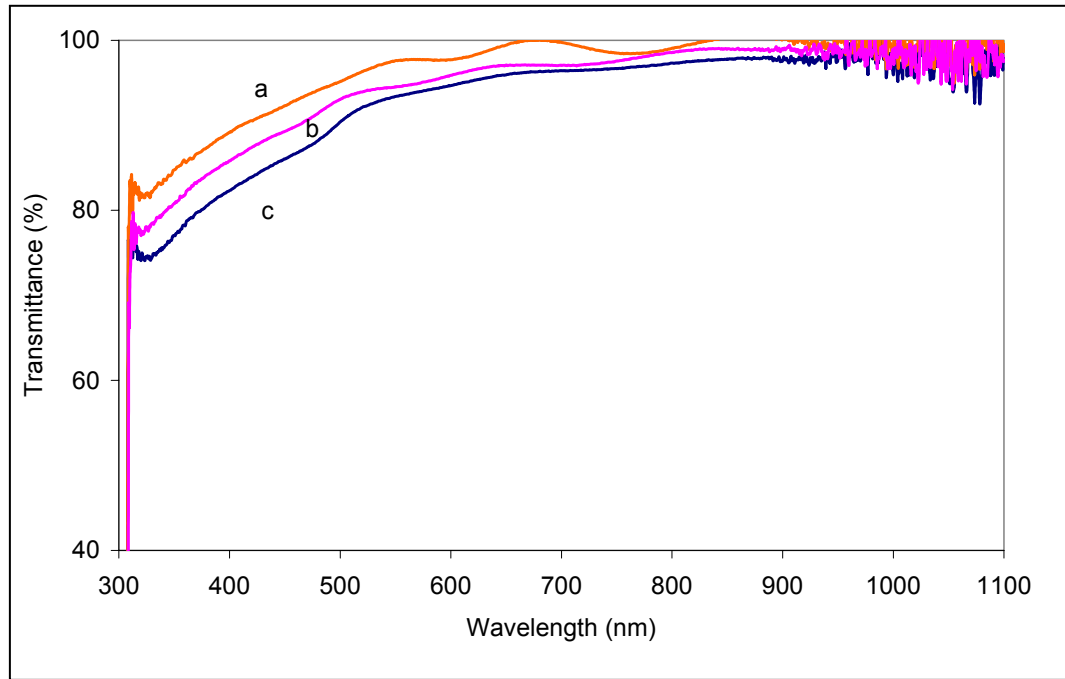


Figure 5.15: Optical transmittance spectra for a single layer deposition of $Zn_xCd_{1-x}S$ films with varying $ZnSO_4$ concentration, (a) 0.04 M (b) 0.02M (c) 0.01 M

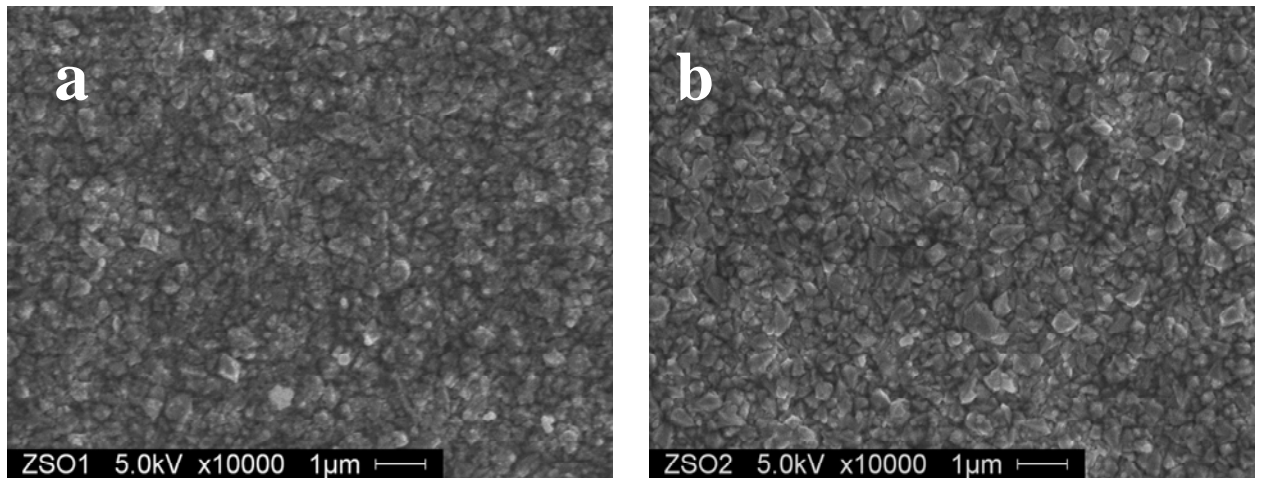


Figure 5.16: SEM micrographs for of the surface of $Zn_xCd_{1-x}S$ film deposited on $SnO_2:F$ glass, for $ZnSO_4$ concentration of (a) 0.01M (b) 0.04M during chemical bath deposition.

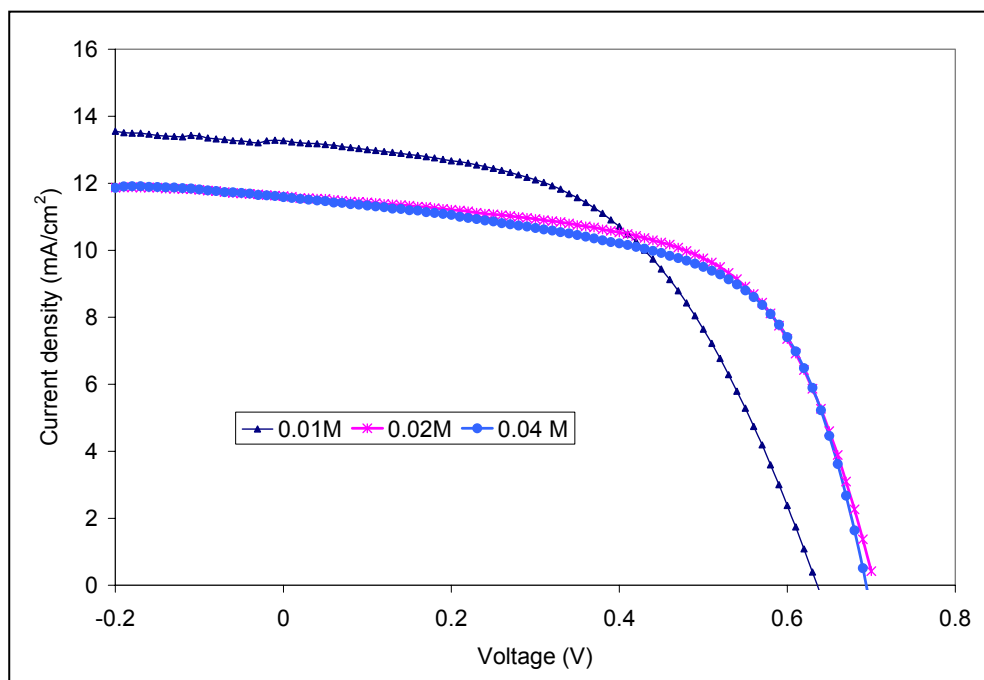


Figure 5.17: The J-V characteristics taken at FSEC for CIGS₂/Zn_xCd_{1-x}S for various concentration of ZnSO₄ in chemical bath.

5.1.5 Thiourea concentration variation

The optical transmittance of the heterojunction partner layer was found to increase as the thiourea concentration was increased (Figure 5.18). This can be explained on the basis of higher extent of conversion of hydroxides to sulfides in presence of higher concentrations of thiourea that acts as sulfide source. This results in higher bandgap of deposited film and consequently the higher transmittance. Higher values of open circuit voltage and short circuit current were obtained for lower concentration of thiourea.

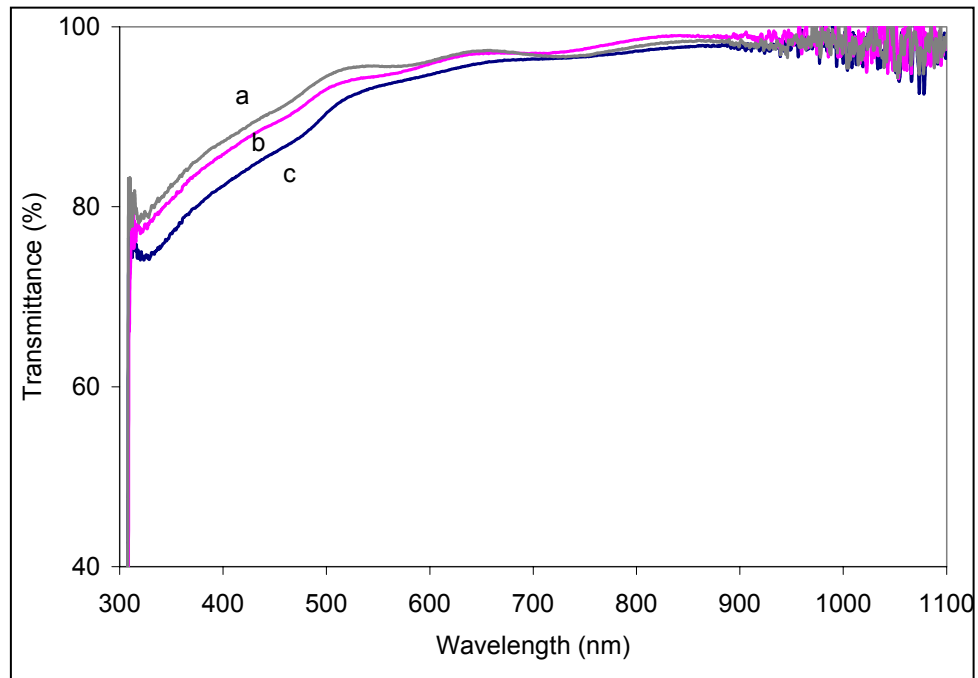


Figure 5.18: Optical transmittance spectra for a single layer deposition of $Zn_xCd_{1-x}S$ films with varying thiourea concentration, (a) 0.375 M (b) 0.25 M (c) 0.125 M

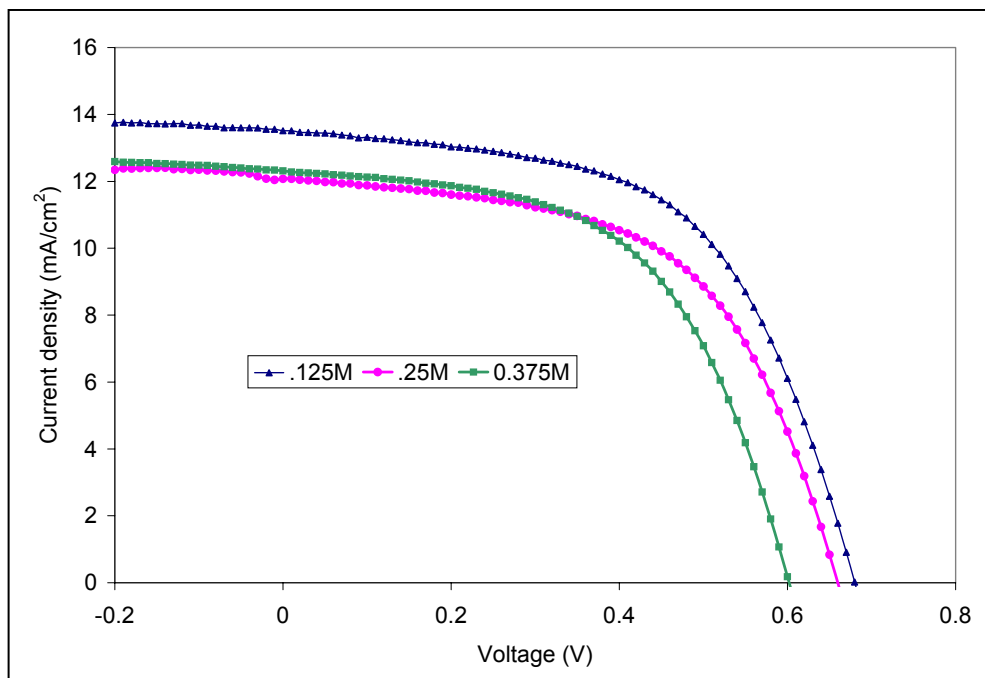


Figure 5.19: The J-V characteristics taken at FSEC for as grown and post annealed CIGS2/
 $Zn_xCd_{1-x}S$ device.

5.1.6 Effect of annealing of $Zn_xCd_{1-x}S$ layer after deposition

The samples were prepared by standard deposition parameters. Afterwards one $Zn_xCd_{1-x}S$ thin film sample was annealed at 200°C for 10 minutes in atmospheric ambient to assist zinc diffusion. The device properties degraded after heat treatment as shown in Figure 5.20. This trend is opposite to the trends observed in CIGS solar cells where Zn diffusion helps to improve the device properties. This difference can be explained based on initial copper-rich CIGS2 growth and subsequent etching of excess copper which result in very low concentration of copper vacancies near surface region. Consequently, the type inversion does not take place. Whereas relatively higher copper vacancies are observed in case of CIGS absorber layer. The vacancies can assist interdiffusion of zinc ions and thus allow zinc to occupy copper site and

creation of Zn_{Cu} . This helps in the formation of buried homojunctions, hence better device properties.

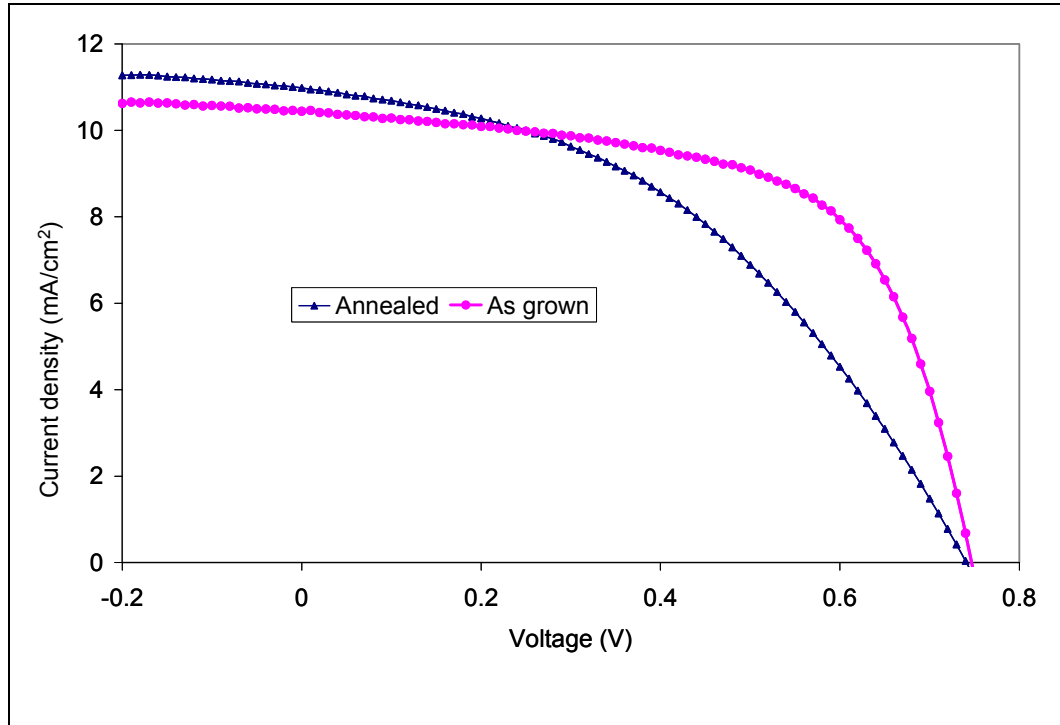


Figure 5.20: The J-V characteristics taken at FSEC for as grown and post annealed CIGS2/ $Zn_xCd_{1-x}S$ device.

5.2 Effect of Indium concentration variation in the absorber layer

The lattice parameter of CIGS2 varies between lattice parameter of $CuGaS_2$ (5.35\AA) to $CuInS_2$ (5.523\AA) depending on $In/(In+Ga)$ ratio. The $In/(In+Ga)$ ratio needs to be optimized to obtain a better lattice match with the heterojunction partner.

The bandgap of the CIGS2 absorber can be increased by reducing the of $In/(In+Ga)$ ratio. With the incorporation of Ga at the near surface region the bandgap increases at the junction and moreover it leads to an elevation of position of the conduction band minimum energy. Thus,

conduction band minimum energy position [43], can be engineered to reach optimum conduction band alignment condition between heterojunction partner and absorber layer and thus to the spike. The smooth transition from CIGS to CdS due to optimum conduction band alignment allows the minority carriers, i.e. electrons to drift from CIGS to CdS regions without hindrance which results in better device properties. However, this proposition needs further investigation, as for the CIGS₂ absorber prepared by sulfurization; the benefit of Ga alloy is limited since most of the Ga added to precursors ends up the rear part of the absorber. This provides the benefit of a back-surface field that repels minority charge carriers electron going to back contact.

In this series of experiments, In/(In+Ga) ratio was varied during the sputter-deposition of metallic precursors. To achieve various indium contents, the thickness of In layer in the metallic precursors was controlled by varying the deposition time . The sputtering system used during the course of this research has a moving substrate mechanism. The thickness of the deposited film is controlled by adjusting the time taken by the substrate to move a unit distance over the sputtering target. Longer duration per unit distance results in thicker layers. Substrate movement durations per inch of 90, 80, 70 and 60 seconds were used. The thickness of Cu-Ga layer was kept constant during this set of experiments. The cell performance for CIGS₂/ Zn_xCd_{1-x}S devices improved with decreasing In deposition time. Highest efficiency of 5.45% was achieved for indium deposition duration per inch of 60 seconds. The maximum short circuit current density of 13 mA/cm² was obtained for the same device. Current-voltage parameters of various solar cells are given in Table III.

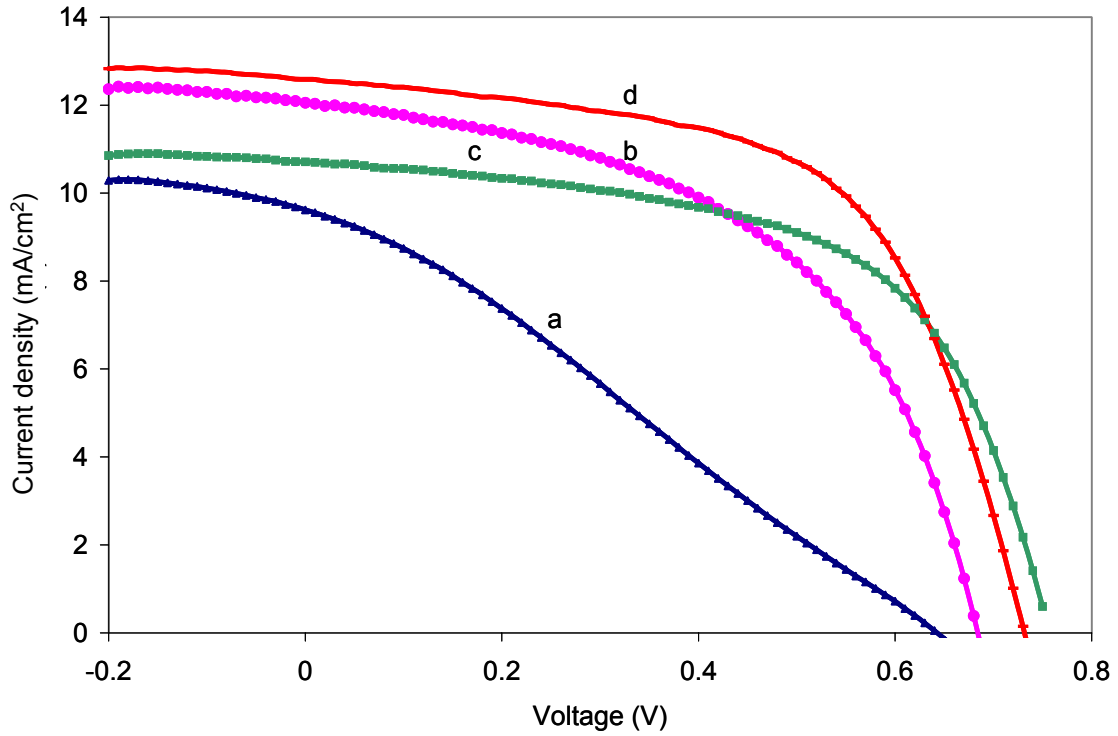


Figure 5.21 The J-V characteristics taken at FSEC for CIGS₂/ Zn_xCd_{1-x}S device formed with various sputtering time for In metallic precursor deposition for absorber layer formation (a) 90 seconds /inch (b) 80 seconds /inch (c) 70 seconds /inch (d) 60 seconds/inch

Table III: Solar cell parameters of CIGS2/ Zn_xCd_{1-x}S thin film solar cell for various In/(In+Ga) ratios (where are the ratio values)

Sample Id	2847_cz	2257_cz	1657_cz	867_cz
Substrate movement duration per unit length (seconds/inch)	45	40	35	30
V _{oc} (V)	0.67	0.68	0.76	0.73
J _{sc} (mA/cm ²)	10.09	12.62	11.21	13.17
V _{mp} (V)	0.49	0.48	0.57	0.53
J _{mp} (mA/cm ²)	7.73	8.80	8.34	10.30
FF(%)	59.34	51.5	58.5	59.45
Efficiency (%)	3.78	4.22	4.767	5.45
R _s (Ω)	26.3	24.8	25.8	25.9
R _p (Ω)	1500	950	1700	1100

X-ray diffraction patterns were obtained for the CIGS2 films deposited with various In deposition times. The chemical composition of CuIn_{0.7}Ga_{0.3}S₂ was calculated from the X-ray diffraction pattern (Figure 5.22) for CIGS2 with In deposition, duration per unit distance of 80 seconds. The lattice constant calculated by linear interpolation of lattice parameters of CuGaS₂ and CuInS₂ was found to be 5.47 Å. Surface analysis by AES indicates Zn/Cd ratio ~4 in the Zn_xCd_{1-x}S film, i.e.; Zn_{0.8}Cd_{0.2}S. Lattice parameter of Zn_xCd_{1-x}S calculated by linear interpolation of lattice constants for ZnS and CdS for Zn/Cd ratio of 4 was found to be 5.49 Å. The percentage difference between the calculated lattice constants for CIGS2 and Zn_xCd_{1-x}S was lower which indicates good lattice match between absorber layer and heterojunction partner

layer. XRD pattern for CIGS2/ $Zn_xCd_{1-x}S$ did not show any peaks of $Zn_xCd_{1-x}S$ possibly because the film was too thin.

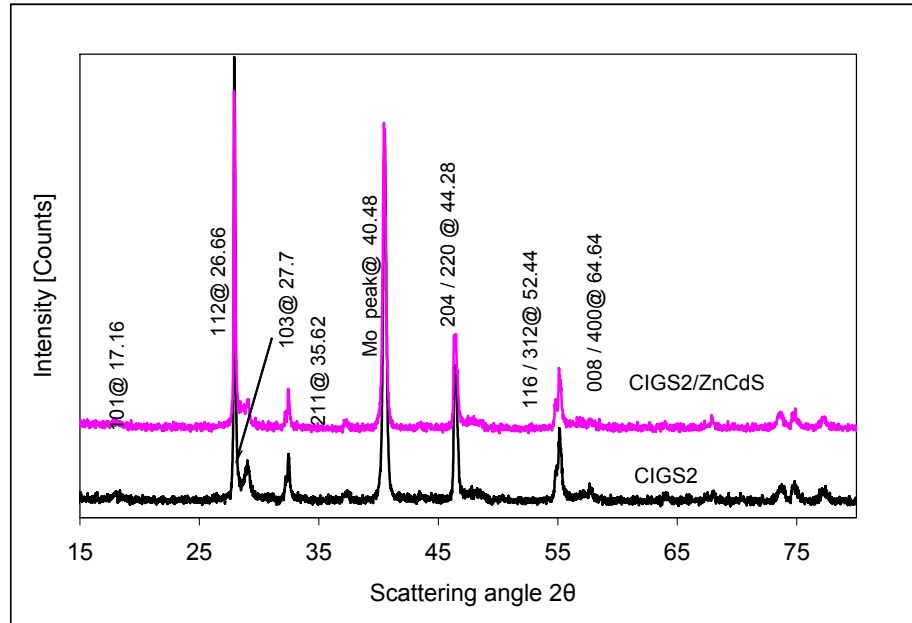


Figure 5.22: X-ray diffraction pattern (θ - 2θ) for CIGS2 absorber layer and CIGS2/ $Zn_xCd_{1-x}S$ layer.

5.3 Comparison of CIGS2/ $Zn_xCd_{1-x}S$ and CdS/CIGS2 solar cell

Figure 5.23 and Figure 5.24 show current-voltage characteristics highest efficiency cell fabricated with $Zn_xCd_{1-x}S$ (#1657CZ) and CdS (#1657C) as heterojunction partners for 2 μm CIGS2 absorber as measured at NREL. The efficiency measured $Zn_xCd_{1-x}S$ as heterojunction partners at NREL was 7.95%, whereas when at FSEC it showed an efficiency of 4.766%. A corresponding increase in efficiencies is expected in all of the results discussed earlier, this is due to the large series resistance of the low-cost probes and the light source consisting of an ELH lamp used at FSEC. Value of the current measured with the probes is lower. CIGS2/ $Zn_xCd_{1-x}S$

has higher open circuit voltage and short circuit current as compared to CIGS2/CdS cell. Whereas the fill factor of CIGS2/ $Zn_xCd_{1-x}S$ cell was lower than that of CIGS2/CdS cell. This can be attributed to the highly resistive ZnS film as compared to CdS. The fill factor can be increased by suitably doping the $Zn_xCd_{1-x}S$ layer so as to enhance its conductivity. Current-voltage parameters for both devices are listed in Table IV. Cells with $Zn_xCd_{1-x}S$ as heterojunction partners demonstrated even higher efficiencies of 5.45% measured at FSEC.

Table IV: Solar cell parameters of CIGS2/CdS (#1657C) and CIGS2/ $Zn_xCd_{1-x}S$ (#1657CZ) thin film solar cell

	CIGS2/CdS	CIGS2/ $Zn_xCd_{1-x}S$
$V_{oc}(V)$	0.7518	0.784
$J_{sc}(mA/cm^2)$	17.522	18.072
$V_{mp}(V)$	0.5703	0.5742
$I_{mp}(A)$	7.21	6.1725
FF(%)	66.34	56.08
Efficiency(%)	8.75	7.95

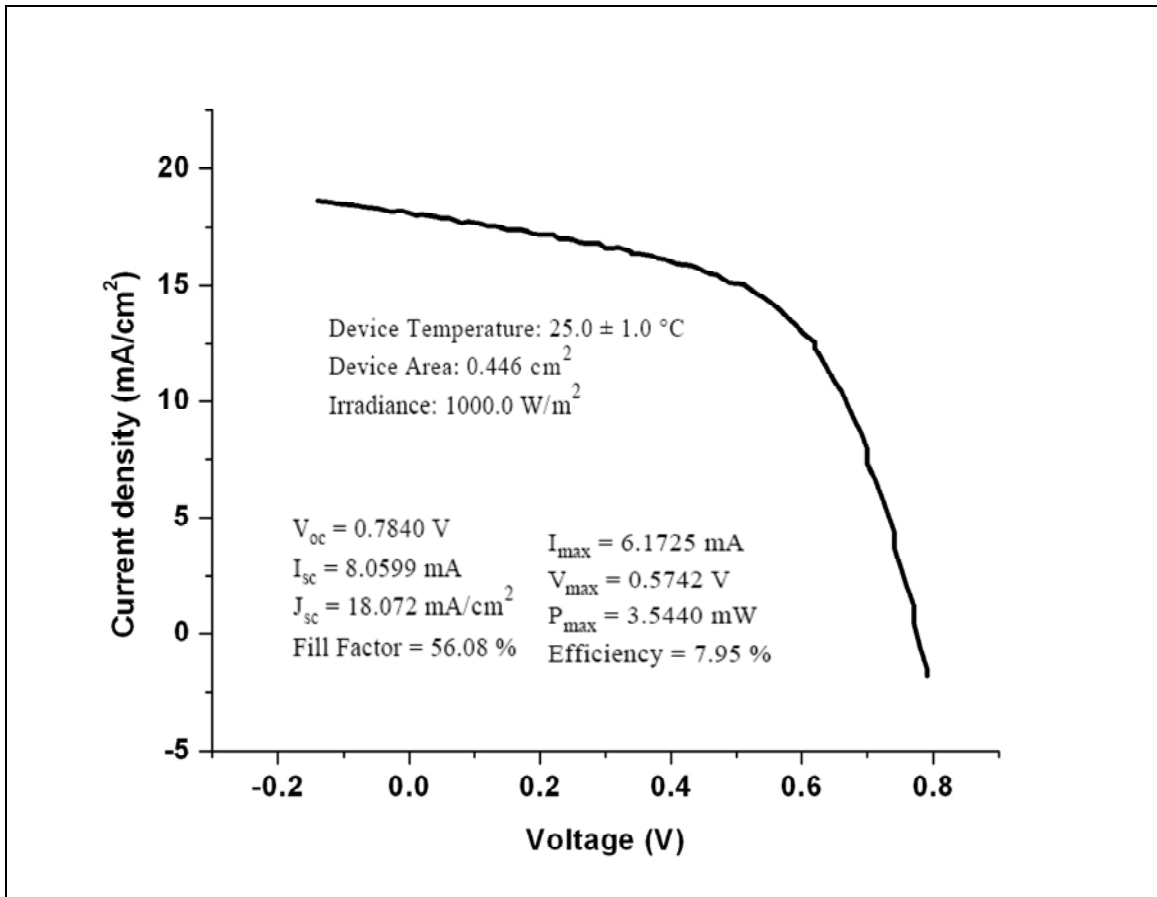


Figure 5.23: The J-V characteristics for SLG/Mo/CIGS2/ $Zn_xCd_{1-x}S$ / i-ZnO/ZnO:Al device (#1657CZ) measured at NREL After 10 minute soak at P_{max} , 5 minute cool.

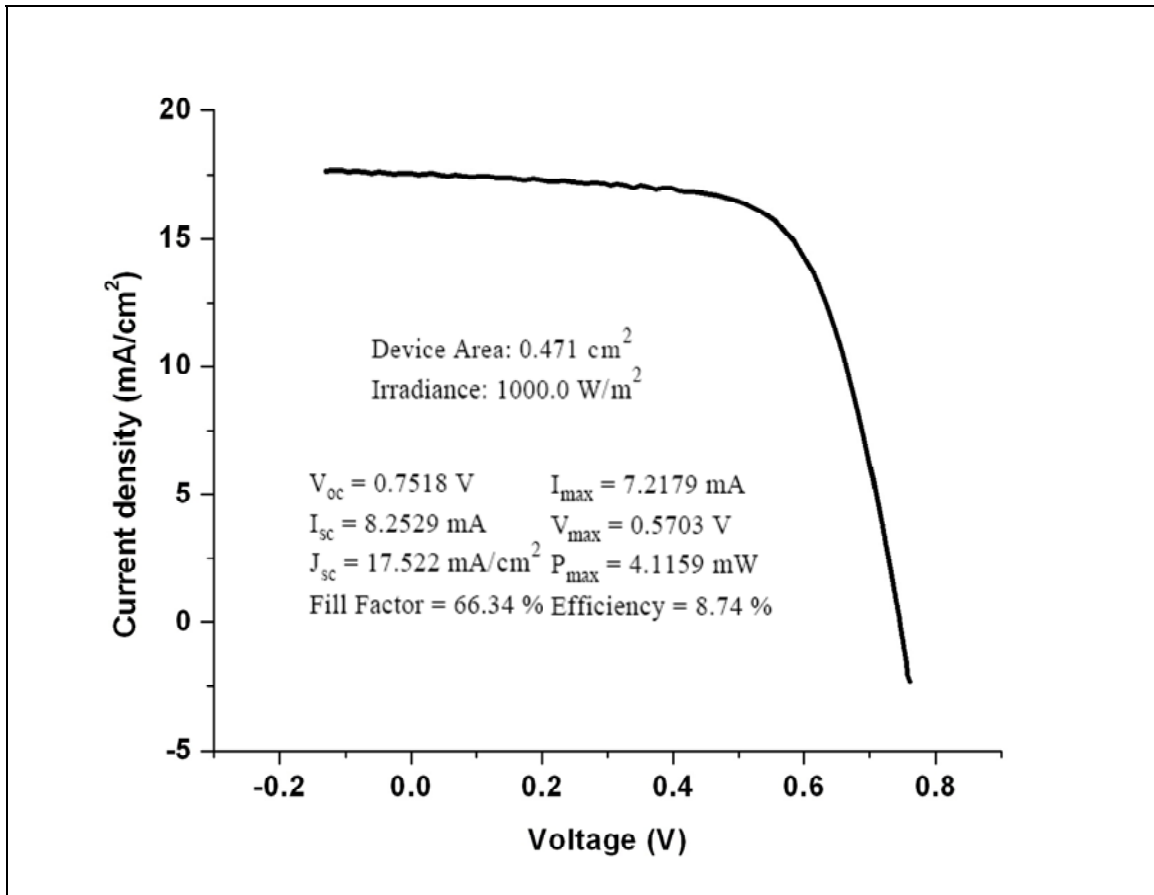


Figure 5.24: The J-V characteristics for SLG/Mo/CIGS2/ CdS / i-ZnO/ZnO:Al device (#1657C) measured at NREL After 10 minute soak at P_{max} , 5 minute cool.

The quantum efficiency measurement at NREL showed gain in blue photon region for SLG/Mo/CIGS2/ $Zn_xCd_{1-x}S$ / i-ZnO/ZnO:Al as compared to SLG/Mo/CIGS2/ CdS / i-ZnO/ZnO:Al, Figure 5.25, which results in higher J_{sc} values.

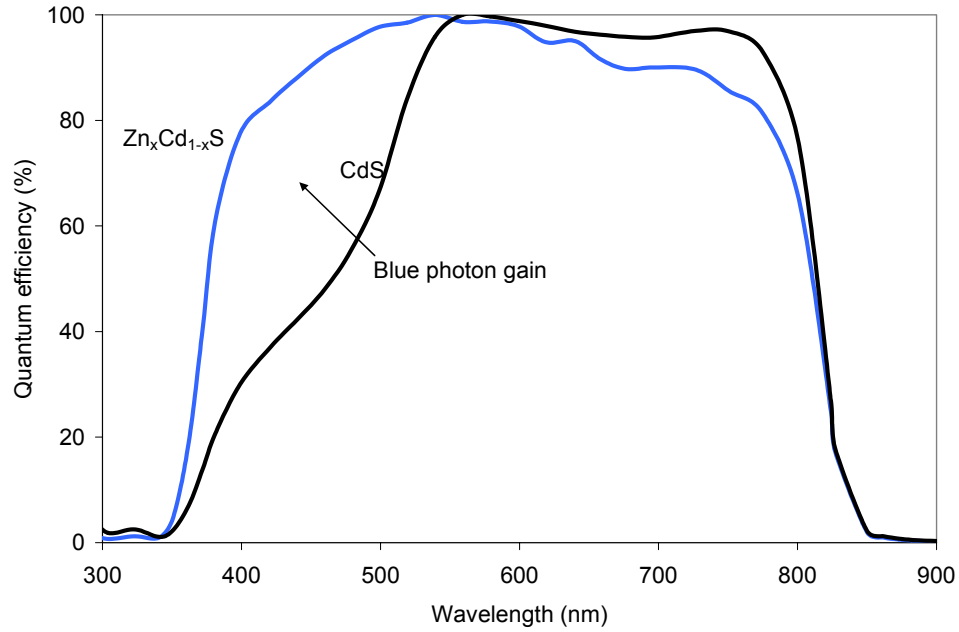


Figure 5.25: Quantum efficiency plot obtained at NREL for SLG/Mo/CIGS2/ CdS / i-ZnO/ZnO:Al (#1657C) and SLG/Mo/CIGS2/ Zn_xCd_{1-x}S / i-ZnO/ZnO:Al (#1657CZ) cells.

5.4 Light-Beam-Induced Current (LBIC) Analysis

Light-beam-induced-current (LBIC) measurements provides a direct link between the spatial non-uniformities inherent in thin-film polycrystalline solar cells, and the overall performance of these cells. Figure 5.26 shows that CIGS2 solar cell fabricated with Zn_xCd_{1-x}S as heterojunction partner has uniformity variations of 3%. Limited uniformity variations indicates good quality cell.

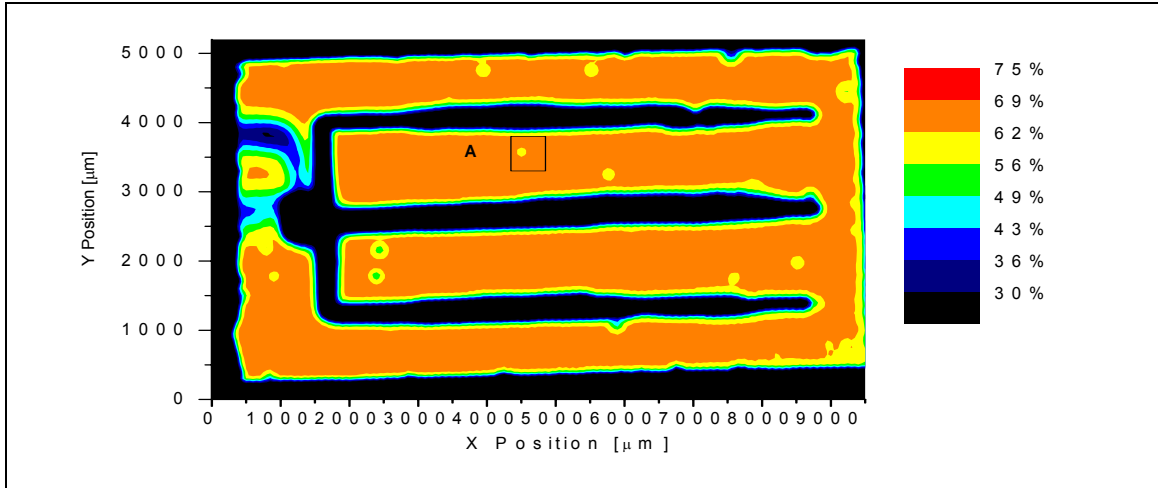


Figure 5.26: LBIC measurements for for SLG/Mo/CIGS2/Zn_xCd_{1-x}S/i-ZnO/ZnO:Al devices (#1657CZ) performed with 638-nm laser measured at Colorado State University.

5.5 Capacitance-Voltage Measurement

The capacitance of junction is given by

$$C = A^2 \epsilon_s / W_d \dots\dots\dots 5.1$$

Where A is the junction width.

$$1/C^2 = [2 / q A^2 \epsilon_s N_A] (V_d - V) \dots\dots\dots 5.2$$

Slope of plot $1/C^2$ versus V gives carrier density. The Capacitance-Voltage measurement of cell #1657CZ was carried out at Colorado State University. The slope of the linear extrapolation of plot shown in gives an average carrier density of $1.6 \times 10^{17} \text{ cm}^{-3}$ [44].

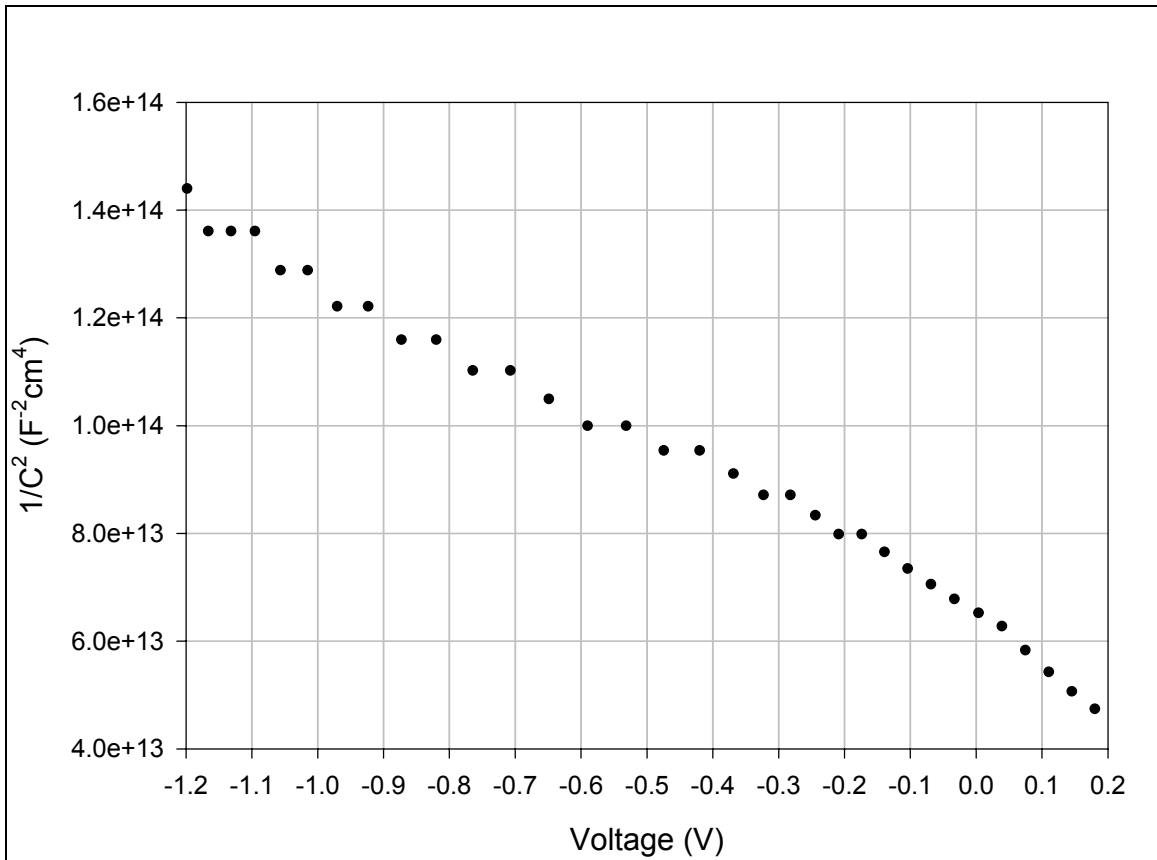


Figure 5.27: shows C^{-2} dependence on voltage. This analysis was carried out at Colorado State University

6 CONCLUSIONS AND RECOMMENDATIONS

The aim of this research was to recommend and develop an alternative heterojunction partner for CIGS2 solar cells. The study has shown that $Zn_xCd_{1-x}S$ is a strong contender as an alternative heterojunction partner. Effect of various chemical bath deposition parameters on device performance was studied and attempts were made to optimize the deposition parameters in order to improve the device performance. Initially $Zn_xCd_{1-x}S$ layer were deposited on $SnO_2:F$ coated glass substrates. The morphological, structural, chemical, and optical properties of $Zn_xCd_{1-x}S$ layer were analyzed using SEM, XRD, XPS, AES, and spectrophotometry techniques. Presence of oxygen in $Cd3d_{5/2}$ and $Zn2p_{3/2}$ core level spectra in XPS analysis indicated that the growth of the film follows cluster mechanism rather than ion-ion mechanism. $Zn_xCd_{1-x}S$ films were then deposited on CIGS2 absorber layer and the device was completed by deposition of the n-type window layer and front contact fingers. Device properties were studied using current–voltage characteristics. Table IV summarizes effects of various constituents of CBD on film growth and device parameter. The device performance of CIGS2/ $Zn_xCd_{1-x}S$ solar cells was comparable to CIGS2/CdS solar cells. This indicates that with further optimization of the deposition parameters of the heterojunction partner and improvement in the absorber layer might lead to better device performance of CIGS2/ $Zn_xCd_{1-x}S$ solar cells as compared to CIGS2/CdS solar cells. Moreover, it should be noted here that all the efforts towards optimization of the deposition parameters were carried out on $\sim 2\mu m$ absorber layer. The crystallinity of the $Zn_xCd_{1-x}S$ layer improved with decreasing pH value of approximately 9.5 of the solution used during the chemical bath deposition. Improved crystallinity resulted in reduction of the series resistance of

the devices. Reduction in the In/(In+Ga) ratio in absorber layer resulted in better device parameters, probably due to better lattice matching and/or due to favorable conduction band alignment.

Table V: Influence of various constituents of CBD on film growth and device parameter

	Parameters				Result summary
	NH ₄ OH [M]	CdSO ₄ [M]	ZnSO ₄ [M]	(NH ₂) ₂ CS [M]	
A	0.09-1.2	0.0002	0.02	0.25	Best at 0.09M eff.=5.07, FF >60% Increasing concentration → decreasing transparency
B	0.58	0.0001- 0.0004	0.02	0.25	for 0.0003M FF>60% Higher R _p , lower R _s
C	0.58	0.0002	.01-.04	0.25	Optimized For~ 0.02M Increasing concentration → Increasing transparency
D	0.58	0.0002	0.02	0.125- 0.375	Decreasing concentration. → higher V _{OC} and J _{SC}

Quantum efficiency plot shows that there is a gain in blue photon response. Higher J_{sc} and V_{oc} with Zn_xCd_{1-x}S as heterojunction partner has been obtained as compared to CdS as heterojunction partner for CIGS2 solar cells. Limited uniformity variations in LBIC studies indicates good quality cell. In this study all the parameters are optimized independently. The near optimized parameters need to be clubbed together to optimize the deposition conditions further.

Further extensive transmission electron microscopy study to find lattice mismatch, electron and X-ray spectroscopy to study band offsets between absorber layer and heterojunction layer with varying Zn/Cd in heterojunction partner and varying In/(In+Ga) ratio in absorber layer will be required to optimize deposition conditions further. Lastly, the $Zn_xCd_{1-x}S$ layer can be doped with suitable dopant to increase the conductance of the layer.

REFERENCE

- [1] The Terawatt Challenge for Thin-Film PV, Ken Zweibel, Aug 2006
- [2] S.M.Sze, "Physics of Semiconductor Devices," Wiley, New York, (1981)
- [3] M. Ruckh, D. Schmid, M. Kaiser, R. Schaffler, T. Walter, and H.W. Schock. Proc. First World Conf. on Photovoltaic Solar Energy Conversion. Hawaii, p.156
- [4] W. E. Devaney and R. A. Mickelsen, "Vacuum Deposition Processes for CuInSe₂ and CuInGaSe₂ Based Solar Cells", Solar Cells, vol. 24, 19, 1988.
- [5] R. W. Birkmire, L. C. DiNetta, P. G. Lasswell, J. D. Meakin, and J. E. Phillips, "High Efficiency CuInSe₂ Based Heterojunction Solar Cells: Fabrication and Results", Solar Cells, vol. 16, 419, 1986.
- [6] J. R. Tuttle, M. A. Contreas, A. M. Gabor, K. R. Ramanathan, A. L. Tennant, D. S. Albin, J. Keane, R. Noufi, Prog. Photovolt.: Res. Appl. 3, 383 (1995).
- [7] N. Tiwari, D.K. Pandya and K.L. Chopra, "Analysis of the photovoltaic properties of sprayed CuInS₂/SnO_x:F solar cells," Sol. Energy Mater. Sol. Cells 15 121-133 (1987). 100
- [8] Onuma, K. Takeuchi, S. Ichikawa, Y. Suzuki, R. Fukasawa, D. Matono, K. Nakamura, M. Nakazawa, and K. Takei, "Preparation and Properties of CuInS₂ in Film Prepared From Electroplated Precursor," Solar Energy, Article In Press, (2005).
- [9] Hodes, T. Engelhard, D. Cahen, L.L. Kazmerski and C.R. Herrington, Presented at the 6th Photovoltaic Solar Energy Conf., (1985).
- [10] A. Antony, A.S. Asha, R. Yoosuf, R. Manoj, and M.K. Jayaraj, Sol. Energy Mater. Sol. Cells, 81 407–417 (2004).

- [11] R.P. Wijesundera and W. Siripala, *Sol. Energy Mater. Sol. Cells*, 81 147–154 (2004).
- [12] T. Watanabe and M. Matsui, *Jpn. J. Apl. Phys. Vol. 35* L1681-L1684 (1996).
- [13] S. Bandyopadhyaya, S. Chaudhuri, and A.K. Pal, *Sol. Energy Mater. Sol. Cells*, 60 323-339 (2000).
- [14] K.Muller, R.Scheer, Y.Burkov, and D.Schmeißer, *Thin Solid Films*, 451 - 452, 120 - 123 (2004).
- [15] N. G. Dhere, S. R. Ghongadi, M. B. Pandit, A. A. Kadam, A. H. Jahagirdar, and V. S. Gade, *IEEE PVSEC*, 876-879, (2002).
- [16] R. Scheer, T. Walter, H. W. Schock, M. L. Fearheiley, and H. J. Lewerenz, *Appl. Phys. Lett.*, Vol. 63, No. 24, 3294-3296 (1993).
- [17] R. Scheer, I.Luck, S. Hessler, H. Sehnert, and H.J. Lewerenz, *IEEE PVSEC*, 1st WCPEC, Hawii, 160-164 (1994).
- [18] R. Scheer, M. Alt, I. Luck, and H.J. Lewerenz, 49 423-430 (1997).
- [19] H. W. Schock, *Thin Film Solar Cells – Next Generation Photovoltaics and Its Application*, Y. Hamakawa, Springer-Verlag Berlin Heidelberg New York (2004).
- [20] H. W. Schock, *Thin Film Solar Cells – Next Generation Photovoltaics and Its Application*, Y. Hamakawa, Springer-Verlag Berlin Heidelberg New York (2004).
- [21] A Rocket, *Cu(In,Ga)(S,Se)₂ Crystal Growth, Structure, and Properties*
- [22] L. L. Kazmerski, *Ins. Phys. Conf. Ser.* **35**, 217 (1997).
- [23] R. R. Potter, C. Eberpacher, L. B. Fabick, in *Conf. Rec. of the 18th IEEE Photovoltaic Special. Conference*, Las Vegas (IEEE, New York, 1985), p. 1659.
- [24] R. W. Birkmire, B. E. McCandless, W. N. Shafarman, R. D. Varrin, in *Proc. 9th E. C. Photovoltaic Solar Energy Conference*, (Kluwer Ed., Dordrecht, 1989), p. 134.

- [25] D. Lincot and J. Vedel, in Proc. 10th E. C. Photovoltaic Solar Energy Conference, (Kluwer Ed., Dordrecht, 1991), p. 931.
- [26] <http://www.semiconductors.co.uk/propivi5410.htm>
- [27] M.A. Contreras, K. Ramanathan, J. AbuShama, F. Hasoon, D.L. Young, B. Egaas and R. Noufi, *Prog. Photovolt: Res. Appl.* 13 (2005), p. 209.
- [28] M. Morkel, L. Weinhardt, B. Lohmüller, C. Heske, E. Umbach, W. Riedl S. Zweigart and F. Karg. *Applied Physics Letters* -- December 31, 2001 -- Volume 79, Issue 27, pp. 4482-4484
- [29] L. Weinhardt, O. Fuchs, D. Groß, E. Umbach, C. Heske, N.G. Dhere, A.A. Kadam, and S.S. Kulkarni, *J. Appl. Phys.* **100**, 024907 (2006).
- [30] I. Hengel, A. Neisser, R. Klenk and M.-Ch. Lux-Steiner, *Thin Solid Films* **361–362** (2000), p. 458.
- [31] R. Klenk, *Thin Solid Films* **387** (2001), p. 135.
- [32] Tokio Nakada, Masashi Hongo, Eiji Hayashi *Thin Solid Films* 431 –432 (2003) 242–248
- [33] M. A. Contreras, T. Nakada, M. Hongo, A. O. Pudov, and J. R. Sites. 3rd World Conf. Photovoltaic Energy Conversion, pages 570–573, 2003.
- [34] T. Nakada and M. Mizutani, *Jpn. J. Appl. Phys.* 41 (2002), Part 2, Nu. 2B, L165- 161.
- [35] T.L. Chu, S.S. Chu, J. Britt, C. Ferekides, C.Q. Wu, *J. Appl. Phys.* 70 (1991) 2688. [36] Von H ortmann and H treptow, *Z. Naturforshg.*, **16a**, 910 (1961)
- [37] D.W.G. Ballentyne and B.Ray, *Physica*, **27**, 337(1961)
- [38] V.D.Vankar, S.R.Das, P.Nath and K.L.Chopra, *Phys. Status.Solidi*, **45**, 665 (1978)
- [39] C.M.Mbow, D.LaPlaze and A. Cachard, *Thin Solid Films*, **88**, 203(1982)
- [40] Y.F. Nicolau, M. Dupuy and M. Brunel. *J. Electrochem. Soc.* Vol. 137, No. 9 (1990), p. 2915.

- [41] R.N.Bhattacharya,K.Ramanathan,L.Gedvilas,B.Keyes,Journal of Physics and Chemistry of Solids 66(2005) 1862–1864.
- [42] J.F. Moulder, W.F. Stickle, P.E. Sobol and K.D. Bomen, Handbook of X Ray Photoelectron Spectroscopy.
- [43] M. Bär, A. Ennaoui, J. Klaer, R. Sáez-Araoz, T. Kropp, L. Weinhardt, C. Heske, H.-W. Schock Ch.-H. Fischer, and M.C. Lux-Steiner Chemical Physics Letters, Volume 433, Issues 1-3, 29 December 2006, Pages 71-74
- [44] Galymzhan T. Koishiyev, James Sites, Bhaskar Kumar, Parag Vasekar and Neelkanth G Dhere, Unpublished.